

JGR Space Physics

RESEARCH ARTICLE

10.1029/2021JA030245

Key Points:

- The sudden ionospheric disturbance (SID) induced by the solar flare (SF) is controlled by the intensity, location, and duration time of the SF
- The SID triggered by the X9.3 SF deteriorates the detection of the cycle slips, thus degrading the accuracy of the kinematic precise point positioning solution
- The X8.2 SF that occurred during the recovery phase of the geomagnetic storm can reduce the precision of GPS measurements

Correspondence to:

T. Xu,
thxu@sdu.edu.cn

Citation:


Nie, W., Rovira-Garcia, A., Wang, Y., Zheng, D., Yan, L., & Xu, T. (2022). On the global kinematic positioning variations during the September 2017 solar flare events. *Journal of Geophysical Research: Space Physics*, 127, e2021JA030245. <https://doi.org/10.1029/2021JA030245>

Received 3 JAN 2022
Accepted 12 AUG 2022

Author Contributions:

Conceptualization: Tianhe Xu
Formal analysis: Adria Rovira-Garcia, Dunyong Zheng, Lingfei Yan
Investigation: Yong Wang
Methodology: Wenfeng Nie, Adria Rovira-Garcia
Supervision: Tianhe Xu
Validation: Lingfei Yan
Writing – original draft: Wenfeng Nie

On the Global Kinematic Positioning Variations During the September 2017 Solar Flare Events

Wenfeng Nie^{1,2} , Adria Rovira-Garcia³ , Yong Wang¹ , Dunyong Zheng⁴ , Lingfei Yan¹, and Tianhe Xu¹ 

¹Institute of Space Sciences, Shandong University, Weihai, China, ²State Key Laboratory of Geo-information Engineering, Xi'an, China, ³Research Group of Astronomy and Geomatics (gAGE), Universitat Politècnica de Catalunya (UPC), Barcelona, Spain, ⁴National-Local Joint Engineering Laboratory of Geo-Spatial Information Technology, Hunan University of Science and Technology, Xiangtan, China

Abstract Several X-class solar flares (SFs) with different intensities and locations on the solar disk occurred in September 2017. Among them, the X9.3 SF on 6 September 2017 was the most intensive SF in the 24th solar cycle. In this study, we investigated and compared the ionospheric response to the different X-class SFs and their impacts on the Global Positioning System (GPS) kinematic precise point positioning (PPP) solutions. We aim to study the mechanism behind the positioning degradation from the perspective of the impacts of the SF-induced ionosphere disturbance on the GPS data processing. By comparing the sudden ionospheric disturbance (SID) induced by the SFs, we observed that the SID is controlled by the intensity, the location, and the duration time of the SF. We found that the SID induced by the SF may deteriorate the cycle slip (CS) detection algorithms seriously. The threshold of the CS detection observables is sensitive to the SID, making the CS easier to be falsely detected. On the other hand, for the SF that occurred during the recovery phase of the geomagnetic storm, as the case of the X8.2 SF, the effects of the SF can reduce the precision of the GPS measurements, thus affecting the positioning accuracy. These mechanisms are essential and significant for the accuracy and stability of the kinematic PPP solution obtained with GPS during the SF events.

Plain Language Summary Solar flares (SFs) are one kind of extreme space weather events, which disturb the radio communication and degrade the precision of the Global Positioning System (GPS). Much efforts have been made to distinguish the different ionosphere responses to the SFs with different intensity and locations on the Sun. However, the positioning performances during the different SFs are less discussed, let alone the mechanism behind the degraded positioning accuracy. In this study, we observed that the sudden ionosphere disturbance (SID) induced by the SF is not only dependent on the intensity and location on the solar disk, but also on the duration time of the SF. We found that the cycle slip (CS) detection algorithms are sensitive to the SID, making the CS easier to be falsely detected. Fortunately, most of the SID effects on the dual-frequency positioning can be mitigated by optimizing the CS detection threshold. On the other hand, the effects of the SF that occurred during the recovery phase of the geomagnetic storm can reduce the precision of the GPS measurements, thus degrading the accuracy of the kinematic precise point positioning solution.

1. Introduction

Solar flares (SFs) are one of the severest solar events, when the Sun releases high-energy protons, electrons, and intense radiation in all wavelengths, affecting not only the Earth's upper atmosphere but also propagation of radio waves. The high-level radiations of X-ray and of the extreme ultraviolet (EUV) radiation result in ionization in the ionosphere on the sunlit side of the Earth. Intense X-ray emission causes absorption in the lower ionospheric D layer, which results in degradation or complete absorption of high-frequency signals. Solar EUV radiation has a decisive impact on the ionospheric heights from 120 to 200 km, and a sudden increase of the EUV emission during SF causes an abrupt enhancement of the ionization that can last from minutes to hours (Donnelly, 1976; Mitra, 1974; Pröls, 2012). The enhanced X-ray photons and the EUV disturb radio communications, degrade the precision of Global Navigation Satellite System (GNSS) measurements, even could damage the Earth-orbiting satellites, and reduce their lifetime (Afraimovich et al., 2008; Cerruti et al., 2006; Chen et al., 2005; Cheng et al., 2018; Demyanov & Yasyukevich, 2021; Desai & Shah, 2020; Sato et al., 2019; Sreeja et al., 2014; Yasyukevich et al., 2018). Therefore, the ionospheric responses to severe SFs are a key topic of study

in the space weather community and considered as an important factor of improving the accuracy and stability of GNSS positioning.

The SF effects on the ionosphere have been studied for many decades, especially with the advent of GNSS (Donnelly, 1976; Hernández-Pajares et al., 1998; Lei et al., 2018; M. Li et al., 2018; W. Li et al., 2018; L. Liu et al., 2011; Mitra, 1974; Tsurutani et al., 2009; Xiong et al., 2011). Tsurutani et al. (2006) discussed the extreme SFs of October 28, October 29, November 4 of 2003, and 14 July 2000 (Bastille Day event) and their photoionization effects on the dayside ionosphere. The largest increase on the dayside ionosphere occurred on the 28 October 2003, where an SF (X17) peaked to 25 TECU (1 TECU equals 10^{16} electron m^{-2} and corresponds to 0.1623 m for the Global Positioning System (GPS) L1 band signal), and not the more intense X-ray flare of 4 November 2003 (X28). The latter event caused only a moderate increase of 5–7 TECU. Since the 4 November SF occurred near the limb of the Sun, the 28 October SF EUV peak flux increase doubled that of the 4 November SF. Then, it was suspected that the solar EUV flux was primarily responsible for the increased total electron content (TEC) in the ionospheric E and F regions during and immediately after SFs. However, other possible contributions may exist.

Many researchers have been devoted to discover the factors that impact the ionospheric response to the SFs in the past decade. Qian et al. (2010) addressed how the location of SFs on the solar disk affects the thermosphere and the corresponding response of the ionosphere. It was found that the X-ray ultraviolet (XUV) radiation dominated ionization in the lower thermosphere, whereas the EUV dominated ionization in the upper thermosphere. Thus, the SF location had a minor effect on the E region and lower thermosphere but had a large effect on the F region ionosphere and upper thermosphere. In fact, the magnitude of sudden ionospheric disturbances (SIDs) increased with the decrease of central meridian distance. Besides, the solar zenith angle was found to be an important factor to determine the distribution of ionospheric disturbances, and case studies as well as statistical studies had reported that the distribution of SIDs presented almost a linear relationship with the cosine value of solar zenith angle (Le et al., 2013, 2016; D. Zhang et al., 2002, 2011). In addition, Qian et al. (2011) found that for SFs with similar magnitudes and the same location on the solar disk, the thermosphere and ionosphere responses showed large variability. The rise time and the decay time following an SF were also important factors in determining the responses.

As for the impacts of the SF-induced ionosphere disturbances on GNSS positioning, numerous studies have reported that the L-band signals of the GPS can be affected, thus degrading the positioning accuracy (Afraimovich et al., 2008; Berdermann et al., 2018; Carrano et al., 2009; Cheng et al., 2018; Demyanov & Yasyukevich, 2021; Desai & Shah, 2020; Dey et al., 2021; Linty et al., 2018; Sato et al., 2019; Sreeja et al., 2014; Yasyukevich et al., 2018). Afraimovich et al. (2008) investigated failures in the GPS performance produced by solar radio bursts with unprecedented radio flux density during the X6.5 and X3.4 SFs on 6 and 13 December 2006, respectively. Significant experimental evidence was found that high-precision GPS positioning on the Earth's entire sunlit side was partially disrupted for 10–15 min on 6 and 13 December 2006. A great number of losses-of-lock (LoL) and carrier-phase cycle slips (CS) resulted from the wideband solar radio noise emission. Berdermann et al. (2018) reported the ionospheric response to the X9.3 flare on 6 September 2017 as well as its impacts on the navigation services over Europe. It was found that the EUV peaks caused strong dynamics in the bottom-side ionosphere, challenging GNSS receivers to maintain signal tracking and, in most cases, to produce satellite LoLs. For the dual-frequency precise point positioning (PPP), deviations of the estimated position in East, North, and Up directions reached 1–2 m. Aiming to address the impacts of the X-class SF on 6 September 2017 on the GNSS, Yasyukevich et al. (2018) reported that the X2.2 and X9.3 SFs did not cause LoLs in the GPS, GLONASS, or Galileo systems, while the positioning errors increased by a factor three in the PPP solution with GPS. By using higher time and frequency resolution of the GNSS and solar radio burst data sets, Sato et al. (2019) found that the rapid EUV and associated ionization enhancement primarily caused the LoLs of the GPS signals. The impact of the radio burst/EUV flare on GNSS positioning was studied using dual- and single-frequency methods, the results of which showed that the dual-frequency solution was more affected by the solar activity than the L1 single-frequency solution. In summary, many efforts have been made to assess the GNSS positioning performances during the SF events and it has been reported that the GNSS signals as well as the positioning accuracies are degraded by SF events.

Recently, Yang et al. (2020) made a comprehensive study of the storm-induced ionospheric disturbance on kinematic PPP solutions using globally distributed GNSS stations during the 2015 St. Patrick's Day storm. Motivated by Yang et al. (2020), we would like to investigate the SF-induced ionospheric disturbance on the global GPS

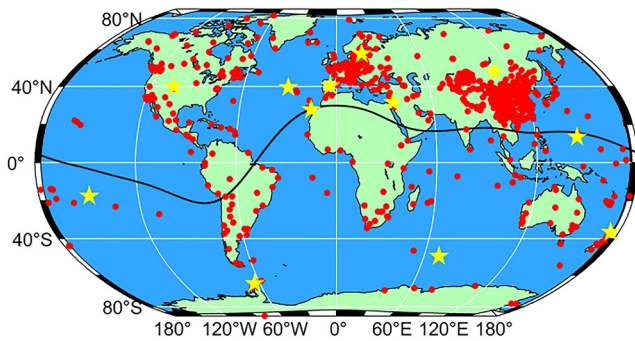


Figure 1. Worldwide distribution of the used GPS stations. The 12 yellow pentagrams represent the selected stations to display the ionosphere responses along the zenith of the stations in the Experiment and Results section. The black solid line indicates the magnetic equator.

kinematic positioning. Though the ionosphere as well as the thermosphere responses to different SFs have been analyzed from cases to cases, the corresponding positioning performances are deserved to be further studied, especially under the SFs with different intensities and locations on the solar disk. In September 2017, four X-class eruptions emerged by the Active Region AR2673 with different intensity and locations. Among them, the X9.3 SF on 6 September 2017 was the strongest SF of the 24th solar cycle. A considerable number of researchers have investigated the ionospheric disturbances as well as the GPS positioning performance associated with this SF (Alfonsi et al., 2021; Berdermann et al., 2018; Blagoveshchensky & Sergeeva, 2019; Desai & Shah, 2020; Fagundes et al., 2020; Imtiaz et al., 2020; Kumar & Kumar, 2020; Lei et al., 2018; M. Li et al., 2018; W. Li et al., 2018; Linty et al., 2018; L. Liu et al., 2020; J. Liu et al., 2021; Nishimura et al., 2021; Owolabi et al., 2020; Qian et al., 2019; Sato et al., 2019; Yamauchi et al., 2018; Yasyukevich et al., 2018; Zakharenkova & Cherniak, 2021; S.-R. Zhang et al., 2019). The novelty of the present study is, on one hand,

to assess and compare the different positioning performances using globally distributed GPS stations during the SFs with different ionosphere responses. On the other hand, we try to discover the mechanism behind the degraded positioning performances from the point view of GPS data processing by considering the ionosphere disturbance effect on GPS signals. This mechanism is essential to mitigate the SF effects on the GNSS positioning.

2. Data and Methodology

2.1. GPS Data

GPS data from the International GNSS Service (IGS) and Crustal Movement Observation Network of China (CMONOC) were processed for the SF effects on GPS kinematic positioning solutions in September 2017. The number of the stations from IGS was about 520, while that from CMONOC was about 250; therefore, a total number of 700+ stations around the world were selected with a sampling rate of 30 s. The distribution of the GPS stations is presented in Figure 1. The 12 yellow pentagrams represent the selected stations to display the ionosphere responses along the zenith of the stations in the Experiment and Results section. It is noted that though most of the stations may also track GLONASS, even Galileo or BDS signals, we only use the GPS data to study the positioning solutions.

2.2. Solar Flare and Ionospheric Disturbance Index

In the present study, X-ray flux was used to represent the characteristics of SFs in September 2017. The 1-min-averaged X-ray data in the wavelength of 0.1–0.8 nm were observed by the Geostationary Operational Environmental Satellite (GOES) 13 and 15. Besides, the solar radio flux at 10.7 cm, as the F10.7 index, was also used to depict the solar space weather condition. In order to evaluate the level of magnetic activity when the SFs erupted, the magnetic storm index, including the Interplanetary Magnetic Field (IMF) components, the longitudinally symmetric disturbances index in the horizontal direction H (SYM-H), and Auroral Electrojet indices were obtained from the Goddard Space Flight Center (GSFC) server.

To measure ionospheric disturbances at the same stations presented in Figure 1, we used the Rate of TEC (ROT), the vertical ROT (vROT), and the ROT Index (ROTI) metrics derived from GPS dual-frequency carrier-phase measurements. By ROT, we mean the variation of the TEC along the line-of-sight from the receiver to the satellite. To describe the ROT along the zenith of the stations, we used the vROT metric. The vROT is weighted by the inverse great-circle distance between the ionospheric pierce points (IPPs) of the satellites and the zenith location of the stations. Defined as the standard deviation of the rate of TEC, the ROTI is an indicator generally used for quantifying small-scale ionospheric plasma irregularities (Cherniak et al., 2014; Pi et al., 1997; Yang & Liu, 2016). These disturbances are expected to generate significant scintillation effects on GPS signals, in such a way that ROTI values can be related to the impacts on kinematic PPP solutions throughout our analysis. We

Table 1
Summary of Data Processing Techniques and Implementations for GPS Dual-Frequency PPP

Item	Techniques and implementations
Observations	GPS dual-frequency code and phase measurements
Processing mode	Forward
Sampling interval	30 s
Elevation mask angle	7°
Cycle-slip detection	Phase Geometry-free and Hatch-Melbourne-Wubbena combination (Blewitt, 1990)
Satellite orbit	Fixed with the final products from IGS with an interval of 15 min
Satellite clock	Fixed with the final products from IGS with an interval of 5 min
Phase center offset	igs08.atx
Ionospheric delay	Ionosphere-free model: First-order effect eliminated by ionospheric-free linear combination
Differential Code Bias	Corrected by PIC1 DCBs from Center for Orbit determination in Europe
Tropospheric delay	The Saastamoinen model for the initial zenith dry and wet delay (Saastamoinen, 1972), along with the GMF projection function (Boehm et al., 2006), and the wet delay is estimated as constant every 2 hr
Solid earth tide, ocean tide loading, and pole tide	IERS Conventions 2010 (Petit & Luzum, 2010); FES2004 (Lyard et al., 2006) for ocean tides
Relativity effect	IERS Conventions 2010

computed ROTIs every 5 min with data sampled every 30 s. It was mapped onto IPPs assuming a thin shell model at an altitude of 350 km.

2.3. GPS Kinematic Positioning Performance

The GPS carrier phase and pseudorange measurements were processed as kinematic PPP solutions by utilizing routines from the Real-Time Kinematic Library (RTKLIB) (Takasu, 2013). In our study, the kinematic positions of the globally distributed GPS receivers were produced every 30 s. An elevation cutoff angle of 7° was used to reduce the multipath effects on the position calculation, while that of 20° was adopted to avoid the geometrical effects as well as the multipath effects on the ROTI calculations (Juan et al., 2018; X. Li et al., 2015; Pi et al., 1997). The detailed data processing techniques and implementations for GPS dual-frequency PPP are summarized in Table 1.

Under normal conditions, the kinematic PPP can achieve decimeter-level accuracy for the receiver with the above processing strategies. In our study, the kinematic PPP solutions were evaluated by a comparison with their daily solutions in a static PPP mode on 3 September 2017. Their position errors were further examined in association with the storm-induced ionospheric disturbances. In addition, we define the positioning convergence by the time that the positioning error converges to 20 cm for the first time and lasts for 10 epochs.

2.4. Cycle Slip Detection Algorithm

Since the CS detection algorithm is critical for the positioning accuracy and stability when extreme space weather events occur, the CS detection algorithm is introduced in the following. In fact, although many CS detection algorithms have been proposed over the past decades, the TurboEdit algorithm is the most widely used in GNSS data processing (Blewitt, 1990). Popular GNSS data processing software, such as GIPSY, Bernese, PANDA, as well as the RTKLIB package used in this study adopts the TurboEdit algorithm or algorithms based on TurboEdit (Bertiger et al., 2020; Dach et al., 2015; J. Liu & Ge, 2003). The TurboEdit algorithm is based on the Hatch–Melbourne–Wubbena (HMW) and Phase–Geometry–Free (PGF) combination observables (Hatch, 1983; Melbourne, 1985; Wubben, 1985). The two basic detection observables can be written as follows:

$$\Delta N_{\text{HMW}} = \Delta\varphi_1 - \Delta\varphi_2 - \frac{f_1\Delta P_1 + f_2\Delta P_2}{\lambda_{\text{HMW}}(f_1 + f_2)} + \Delta\xi_{\text{HMW}} \quad (1)$$

$$\Delta\varphi_{\text{PGF}} = \lambda_1\Delta\varphi_1 - \lambda_2\Delta\varphi_2 = \lambda_1\Delta N_1 - \lambda_2\Delta N_2 + (\gamma - 1)\Delta I + \Delta\xi_{\text{PGF}}$$

where Δ is the difference operator between two consecutive epochs, which are separated 30 s in the present study and λ_{HMW} is the wide-lane wavelength of 86 cm; p_j in the unit of meter and φ_j in the unit of cycle are the pseudorange and carrier phase at frequency f_j , respectively; I is the line-of-sight ionospheric delay at frequency f_1 in the unit of meter; γ is the frequency-dependent multiplier factor ($\gamma = (f_1/f_2)^2$); it is noted that for the ionosphere-free (IF) combination, the factor is nearly zero; λ_j is the carrier wavelength at frequency f_j in the unit of meter; N_j is the phase ambiguity in the unit of cycle; ξ is the combination of measurement noise and multipath error for pseudorange and carrier phase observations in the unit of meter.

To detect the CS by the TurboEdit algorithm, the commonly used threshold for the HMW observable is from 1 to 2 cycles of λ_{HMW} (i.e., 0.86–1.72 m), while that for the PGF observable is from 0.05 to 0.15 m (X. Zhang et al., 2014). The RTKLIB package used in the present study sets as a default threshold of the PGF observable to 0.05 m (Takasu, 2013). We will show in the Experiment and Results section that, with the default thresholds, the kinematic PPP can achieve accurate and stable performance under ionospheric quiet conditions.

3. Experiment and Results

3.1. Solar Flare Conditions in September 2017

September 2017 was an active space weather period in which many SFs and two geomagnetic storms occurred. The stormy conditions were driven by the Active Region AR2673, from which four X-class eruptions emerged. Especially, the period from September 3 to 13 September 2017 gave us an insight into solar-terrestrial interaction and allowed us to study its influence on GPS positioning in more detail. In the following, we briefly describe such an interesting solar activity period.

Figure 2a depicts the X-ray measurements recorded by the primary (G15) and secondary (G13) GOES satellites. We can distinguish between the two channels 0.1–0.8 nm (G15: brown; G13: blue), indicating the well-known flare size in the X-ray range, and 0.05–0.4 nm (G15: light brown; G13: light blue). Figure 2b depicts that the F10.7 measurements from September 3 to September 10 were all larger than 90 sfu; therefore, the solar space weather condition was quite active during the period. The occurrence information of the X-class SFs during the September 6–10, 2017 space weather event is summarized in Table 2. It is noted that the X9.3 class SF was the strongest eruption in more than a decade.

Besides, the strongest X9.3 flare on September 6 triggered also a geoeffective CME event, which triggered disturbed magnetospheric and ionospheric conditions, as depicted in Figure 2c. Two sequential geomagnetic storms peaked on September 8, the first with a SYM-H minimum value of -146 nT, observed at 01:08 UT, and the second with a SYM-H minimum of -112 nT at 17:08 UT. The sequence of these events was in accordance with the time line of the SF effects as described in Tsurutani et al. (2009).

In the following, we focused on the main event of this solar activity phase, the X-class SF on September 6 and 10 September 2017, and we follow their effects on the ionosphere down to application examples in the kinematic positioning domain.

3.2. Ionospheric Response on 6 September and Kinematic PPP Error

We study the response of the ionosphere to the SFs on 6 September from the point view of the aforementioned ROTI in Figure 3. To complement the time series of ROTI, we include the vROT along the zenith of each station. To distinguish the SF effects on the sunlit side of the Earth, we selected and displayed the ionosphere responses at 12 stations according to their longitude distribution. The distribution of the 12 stations is depicted as yellow pentagrams in Figure 1.

From Figure 3, we can see fluctuations of the vROT series at around 9:00 UT and 12:00 UT, the time of which was consistent with the peak eruption of the X2.2 and X9.3 SF on the day. The vROT fluctuation is a typical phenomenon of the SID due to the SF. In detail, the amplitude of the vROT fluctuation at around 9:00 UT was about 0.2 TECU/min while that at around 12:00 UT was about 1.5 TECU/min. The difference of the fluctuation amplitude revealed the effects of the different magnitude of the X-class SF on the ionosphere. Besides, we can find that not all of the selected stations showed the vROT fluctuations during the SF events. Taking the vROT fluctuation at around 12:00 UT as an example, the apparent fluctuations occurred for stations whose

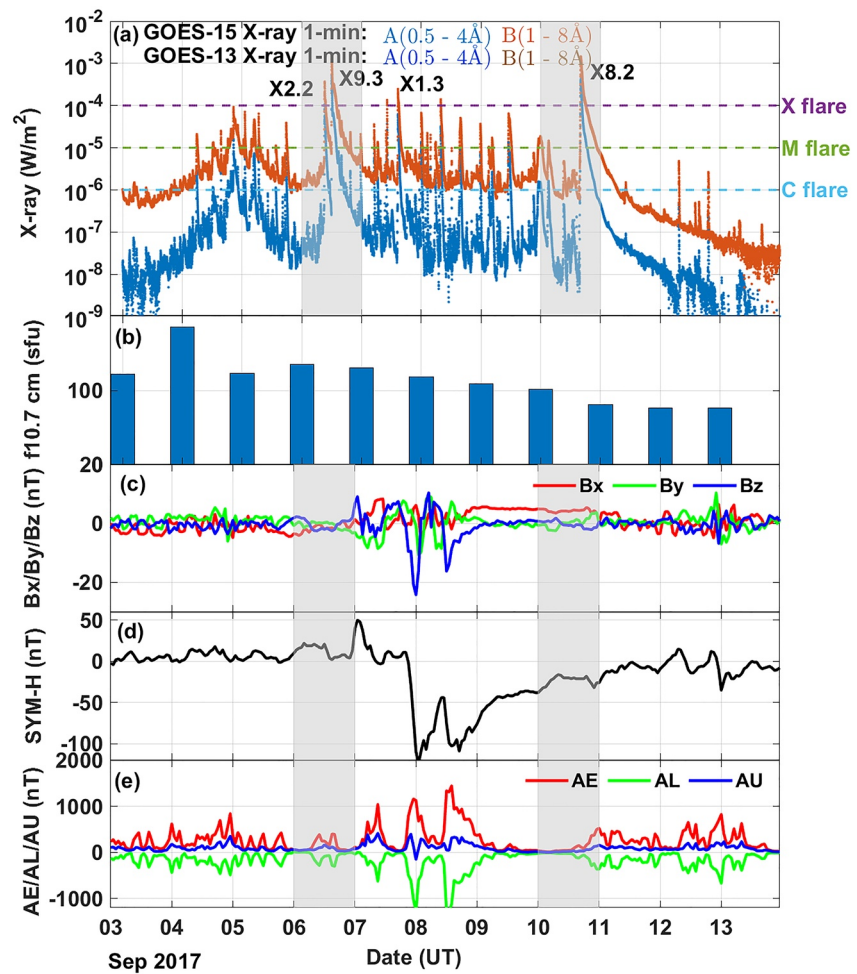


Figure 2. The time series of (a) the X-ray flux from GOES satellites; (b) F10.7 solar flux; (c) IMF B_x , B_y , and B_z components; (d) the geomagnetic SYM-H index; and (e) auroral electrojet AE/AL/AU indices during September 3 to 13 September 2017. The shaded areas highlight 6 and 10 September when the X-class SF events occurred.

longitudes were from 71.9 W to 70.2 E. Combining the distribution of the 12 stations within the earth terminator in Figure 4b, we deduced that the stations with apparent vROT fluctuation were experiencing the sunlit period.

Figure 4 presents the global temporal-spatial variations of ROTI during the X2.2 and X9.3 SF on 6 September 2017. Specifically, we plotted the Earth terminator, separating the day side and night side. The 12 stations in Figure 3 are also presented in Figure 4.

Figure 4a depicts the variations of ROTI from 08:55 UT to 09:20 UT on a global scale when the X2.2 SF occurred. Since the ROTI was calculated at a 30 s rate over 5 min, the time title above the subfigures identifies the start time of the window computing the ROTI. From Figure 4a, we can see that the global distribution of the

Table 2
Summary of the SF Occurrence Information During the September 6–10 2017 Space Weather Event

Class	Date 2017	Start (UT)	Max (UT)	End (UT)	Risetime (min)	Decay time (min)	Duration (min)
X2.2	6 September	08:57	09:10	09:17	13	7	20
X9.3	6 September	11:53	12:02	12:10	9	8	17
X1.3	7 September	14:20	14:36	14:55	16	19	35
X8.2	10 September	15:35	16:06	16:31	31	25	56

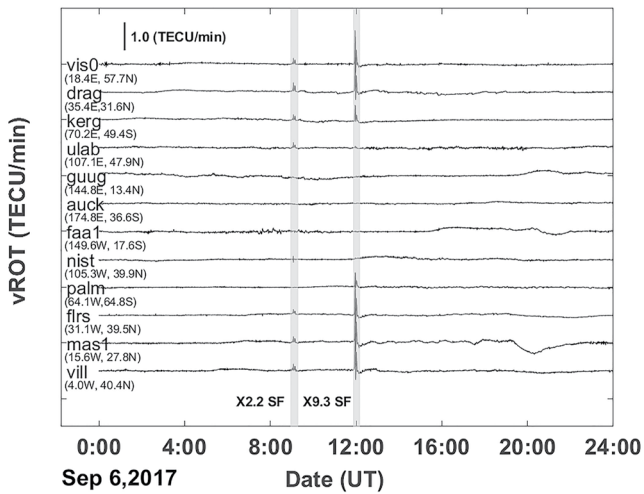


Figure 3. The time series of vROT along the zenith of the stations on 6 September 2017. Twelve stations around the world were selected and displayed according to their longitude distribution. The shaded areas represent the occurrence time of the X2.2 and X9.3 SF.

ROTI was around 0.1 TECU/min most of the time. From the point of the spatial variations, ROTIs at the high latitude were larger than that at any other area. Numerically, Figure 4a shows that the magnitude of the ROTI at the high latitude in the northern hemisphere was around 0.2 TECU/min. This can be explained by the complex particle precipitation in the high-latitude area (Juan et al., 2018). In addition, we can see a quite apparent increase of the ROTI, due to the almost instant photoionization, to the magnitude of 0.25 TECU/min in the snapshot of 09:00 and 09:05 UT during the dayside when the X2.2 SF erupted.

Correspondingly, Figure 4b depicts the variations of the global ROTI from 11:45 to 12:10 UT during which time the X9.3 SF occurred. The largest difference of the ionospheric response to the X2.2 SF in Figure 4a and X9.3 SF in Figure 4b was the magnitude of the ROTI increase. From Figure 4b, we can see that the ROTI increased apparently to the magnitude of more than 0.5 TECU/min from 11:55 UT and decayed at 12:05 UT. And we can find that the variations of the ROTI in Figure 4 were consistent with the vROT fluctuations in Figure 3, indicating the different level of the ionospheric responses to the different X-class SF.

We now turn our attention to the kinematic PPP solutions producing positioning errors during the SF events depicted in Figure 5. Since the sampling rate of the GPS data was 30 s, we computed the root mean square (RMS) of the

positioning errors every 5 min to match the ROTI analysis. The time description above the subfigures in Figure 5 indicates the start time of the 5 min window to compute the 3-Dimension (3D) RMS of the positioning errors.

From Figure 5a, we can see that the positioning errors during the selected time were quite stable. The 3D RMS positioning errors of most of the stations ranged from 0.10 to 0.20 m. By comparing with Figure 4a, when the ionospheric response at 09:00 UT on the dayside increased, the positioning errors did not experience large variations in Figure 5a. On the contrary, in Figure 5b, positioning errors increase from 11:55 UT, the time of which was consistent with the vROT fluctuation and ROTI variations in Figures 3 and 4. From Figure 5b at the snapshot of 11:45 UT and 11:50 UT, we can see that the positioning errors were at the same magnitude as that in Figure 5a. However, when the ROTI varied starting from 11:55 UT, the positioning performance severely deteriorated. The 3D RMS positioning errors for most of the stations on the dayside increased to more than 0.5 m, while those in the night side did not vary as expected.

Therefore, the positioning errors in Figure 5 indicated the effect of the different level X-class SF on the positioning accuracy. The positioning errors in Figure 5 may suggest that the kinematic PPP solution can cope with the effect of the X2.2 SF rather than the X9.3 SF. It is worth noting that the SF classes are given in logarithmic units; therefore, the difference between the X2.2 and X9.3 SF is quite huge. In the Discussion section, we tried to analyze the reasons behind the positioning accuracy reduction during the two X-class SFs.

3.3. Ionospheric Response on 10 September and Kinematic PPP Error

We now proceed with the analysis of 10 September 2017. In the same way as in Figure 3, Figure 6 depicts the time series of the vROT along the zenith of the stations on 10 September 2017 for the same 12 stations.

Figure 6 depicts that most of the time the vROT varied below 0.1 TECU/min. At around 16:00 UT, when the X8.2 SF erupted, the magnitude of the vROT reached 0.2 TECU/min for stations from about 149.6 W to 18.4 E. It is interesting to note that the magnitude of the vROT fluctuation during the X8.2 SF on September 10 was at the same level as that during the X2.2 SF on September 6. The small fluctuation of the ROT during the X8.2 SF leads to the inconspicuous ROTI variations at the level of about 0.1 TECU/min as can be seen from Figure 7.

The 3D positioning errors of the kinematic PPP solutions during the X8.2 SF are depicted in Figure 8. Different from the inconspicuous ROTI variations in Figure 7, we can see apparent positioning accuracy degradation from 15:50 to 16:15 UT on the dayside in Figure 8. Numerically, the 3D RMS of the positioning errors varied from 0.1 to 0.5 m during the occurrence of the X8.2 SF.

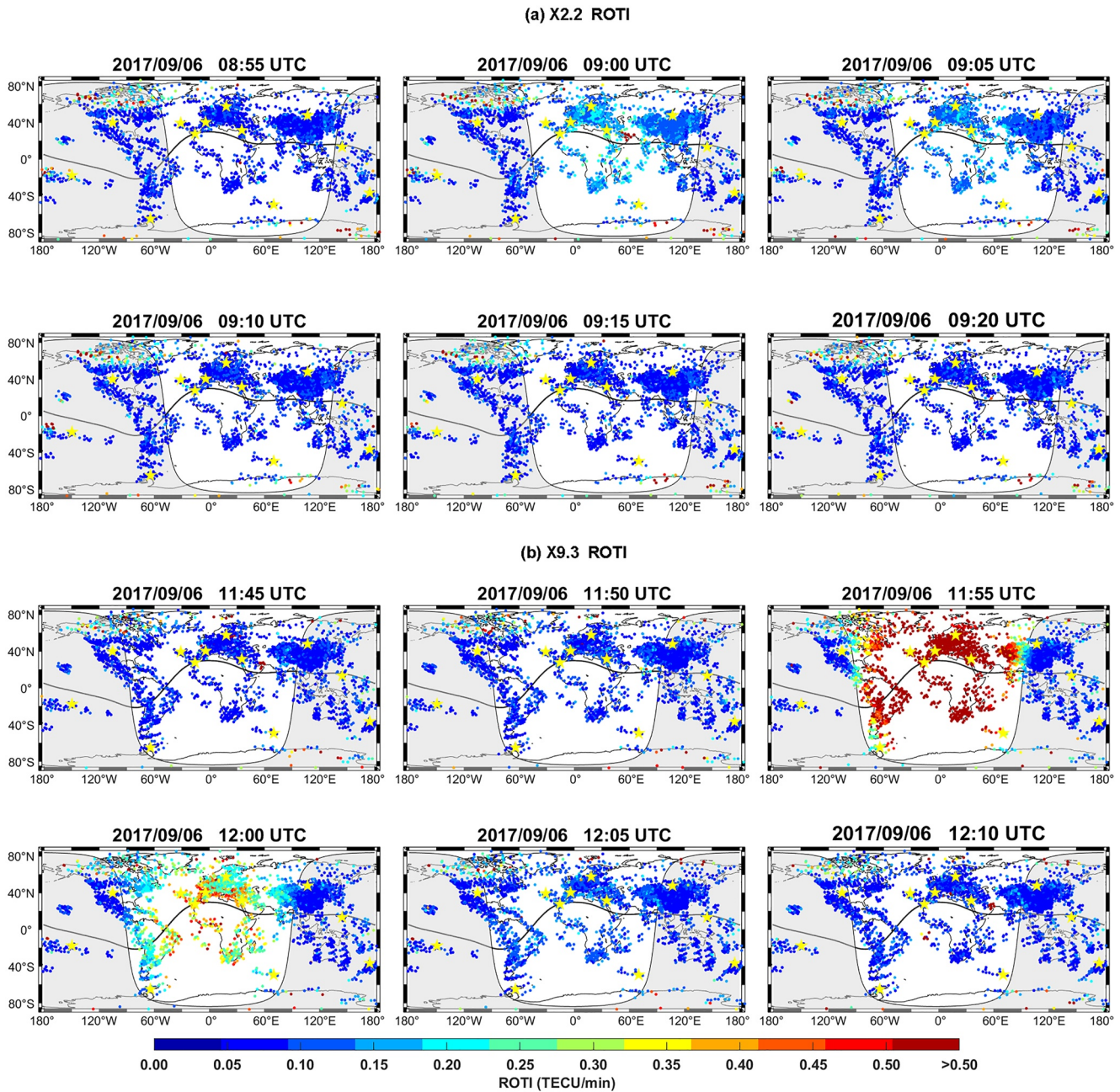


Figure 4. Snapshots of global temporal-spatial variations of ROTI during the (a) X2.2 SF and (b) X9.3 SF on 6 September 2017. The gray shade indicates the night side. The black solid line represents the magnetic equator. The 12 yellow pentagrams represent the selected stations to display the ionosphere responses along the zenith of the stations in Figure 3. The CS threshold of the PGF observable is 0.2 m when computing the ROTI.

Comparing the positioning errors during the X9.3 SF in Figure 5b with that during the X8.2 SF in Figure 8, we can find that the pattern and distribution of the PPP errors were different. In the case of the X8.2 SF, the positioning accuracy degradation occurred the whole interval from 15:50 UT to 16:15 UT. When the eruption of the X8.2 SF reached the maximum intensity at 16:06 UT, the positioning errors did not increase. Furthermore, the distribution of the magnitude of the positioning errors during the X8.2 SF was not as even as that during the X9.3 SF. For example, at 16:05 UT in Figure 8, most of the 3D RMS of the positioning errors in Europe were below 0.1 m, while that in north and South America ranged from 0.2 to 0.45 m. In contrast, at 12:00 UT in Figure 5b, most of the 3D RMS of the positioning errors in Europe, Africa, as well as South America were over 0.5 m.

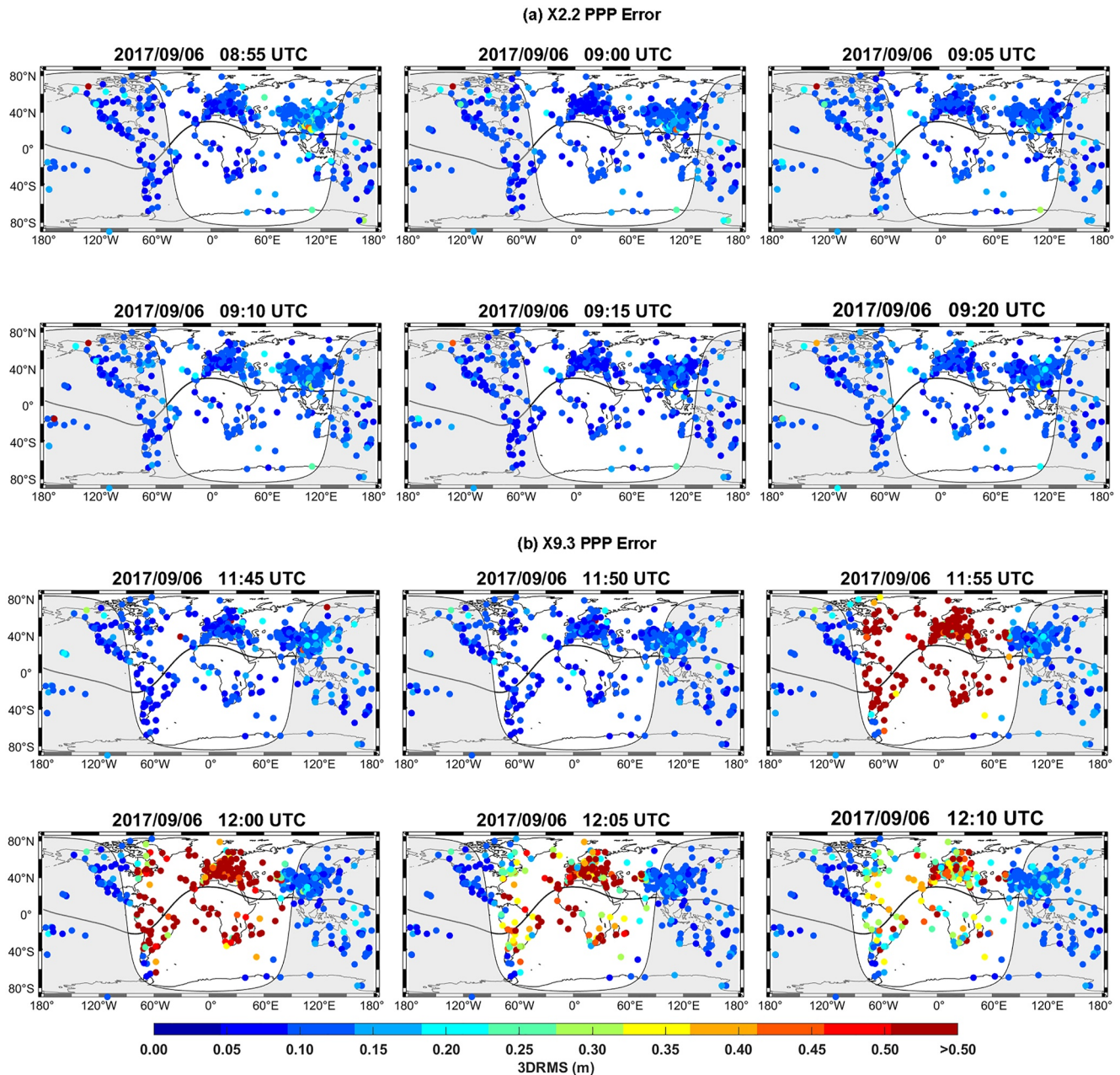


Figure 5. Snapshots of 3D kinematic PPP errors during (a) X2.2 SF and (b) X9.3 SF on 6 September 2017. The gray shading indicates nightside. The black solid line represents the magnetic equator.

4. Discussion

4.1. The Factors That Impact the Ionospheric Response to the SF

The different ionospheric responses to the X2.2 and X9.3 SFs that are depicted in Figures 3 and 4 indicate that the greater magnitude of the SF is, the greater the impact on the ionosphere. However, this is not the case for the ionospheric responses to the X8.2 SF on 10 September 2017 in comparison to the X2.2 SF and X9.3 SF on 6 September 2017. We expected that the v ROT fluctuation and ROTI variation during the X8.2 SF should be almost the same level as those during the X9.3 SF. In fact, the results in Figures 6 and 7 show that the magnitude level of the v ROT fluctuation during the X8.2 SF was comparable to that during the X2.2 SF, while the ROTI

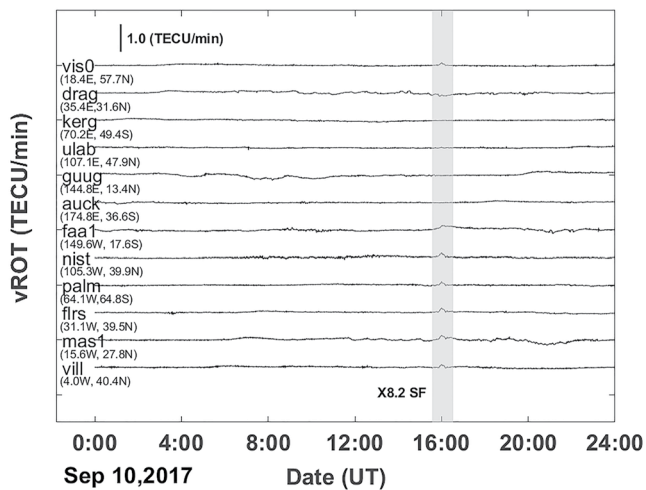


Figure 6. The time series of vROT along the zenith of the stations on 10 September 2017. The 12 stations are the same as those in Figure 3. The shaded area represents the occurrence time of the X8.2 SF.

variation during the X8.2 SF was not even stronger than that during the X2.2 SF. Therefore, there should be some other factors that impact the ionosphere.

We assessed the differences among the three X-class SFs; although originated from the same active regions of AR2673, the locations of the SFs were different as depicted in Figure 9. The two largest flares with similar magnitudes were a disk flare (X9.3 SF on 6 September 2017) and a limb flare (X8.2 SF on 10 September 2017), respectively.

The response of the Thermosphere-Ionosphere system during SFs is controlled by many factors, including the location of an SF on the Sun (Qian et al., 2010; D. Zhang et al., 2011). Although soft X-ray enhancement is not affected by the SF location, EUV enhancement in disk flares is much larger than in limb flares of the same magnitude, especially in the wavelengths longer than 30 nm. This larger enhancement in the EUV for a disk flare was related to the difference in the optical thickness of the soft X-rays and EUV in the solar atmosphere.

Interplanetary Coronal Mass Ejection (ICME), which dominated the soft X-ray spectrum, is generally optically thin in the solar atmosphere. The amount of the soft X-ray that is absorbed when it travels through the solar atmosphere does not change much when the location of an SF changes from

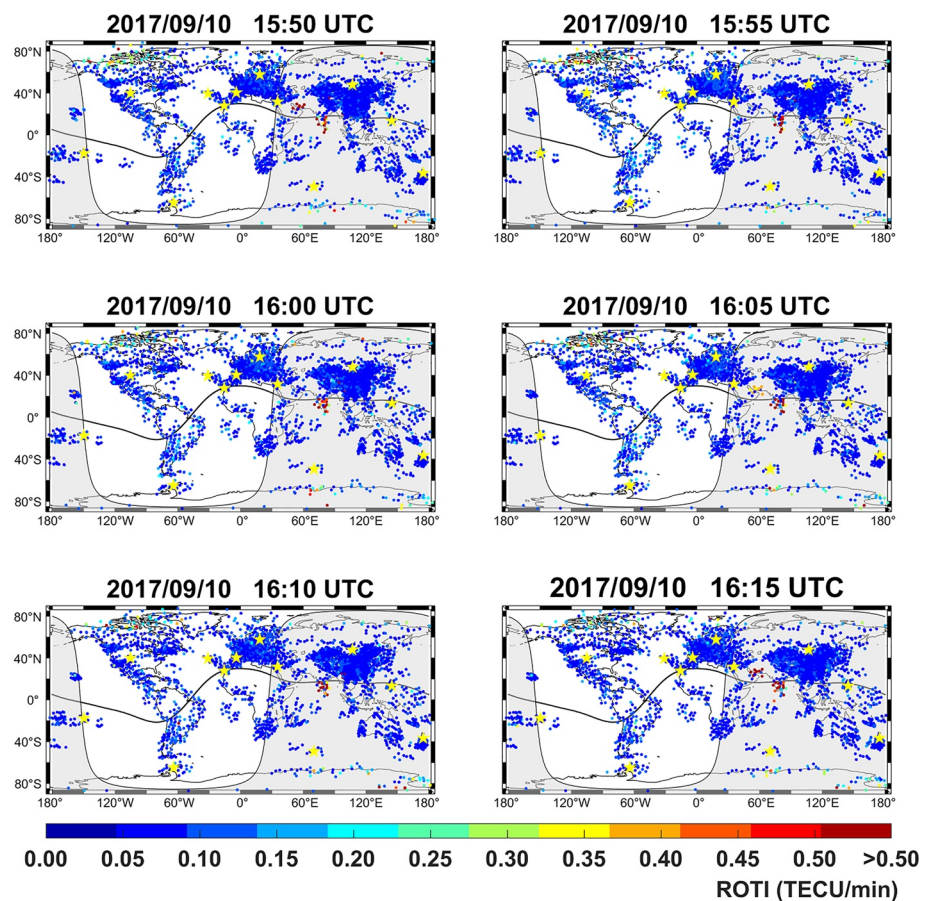


Figure 7. Snapshots of 5 min ROTI during the X8.2 SF on 10 September 2017. The gray shading indicates nightside. The black solid line represents the magnetic equator. The 12 yellow pentagrams represent the selected stations to display the ionosphere responses along the zenith of the stations in Figure 3 and Figure 6. The CS threshold of the PGF observable is 0.2 m when computing the ROTI.

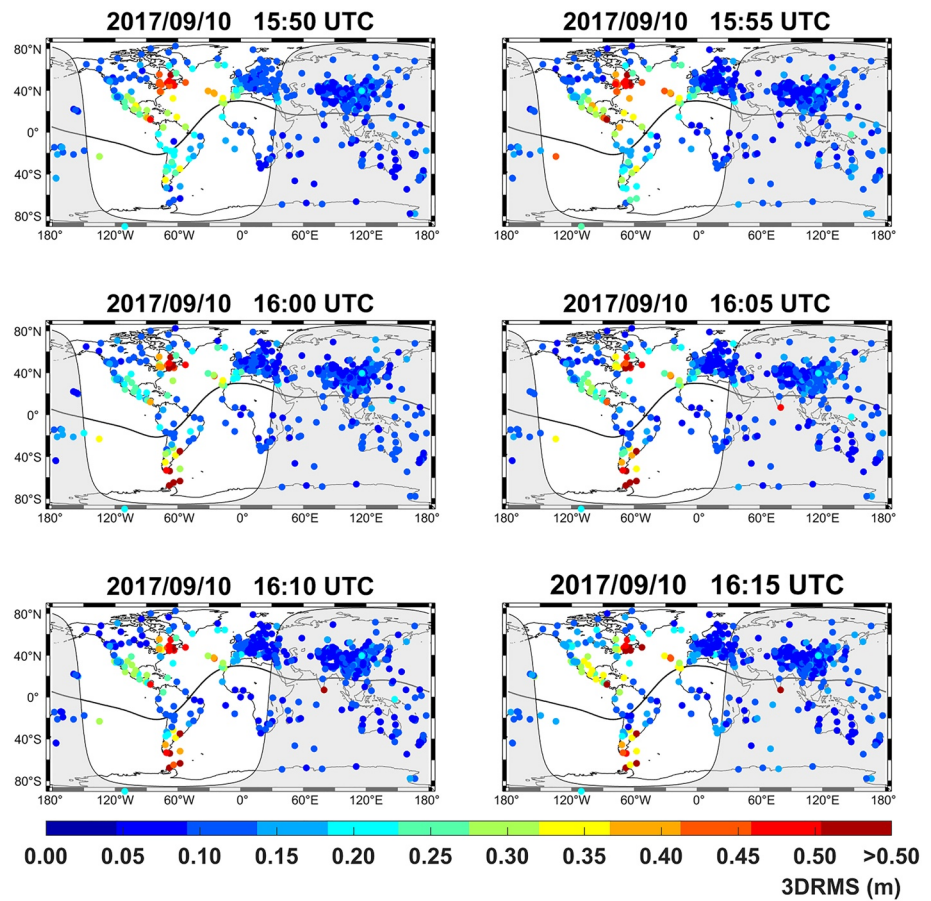


Figure 8. Snapshots of 3D kinematic PPP errors during the X8.2 SF on 10 September 2017. The gray shading indicates nightside. The black solid line represents the magnetic equator.

the center to the limb. Chromospheric emissions, which dominated the EUV spectrum, are often optically thick in the solar atmosphere. Absorption of optically thick emissions was greater if an SF occurs on the limb due to the longer optical path length. Therefore, limb flares imply less enhancement at EUV wavelengths.

Figure 10b depicts the EUV observations from SOHO in the wavelengths of 26–34 nm and 0.1–50 nm. As it can be seen, both EUV fluxes during the X8.2 limb flare on 10 September 2017 were much larger than those during

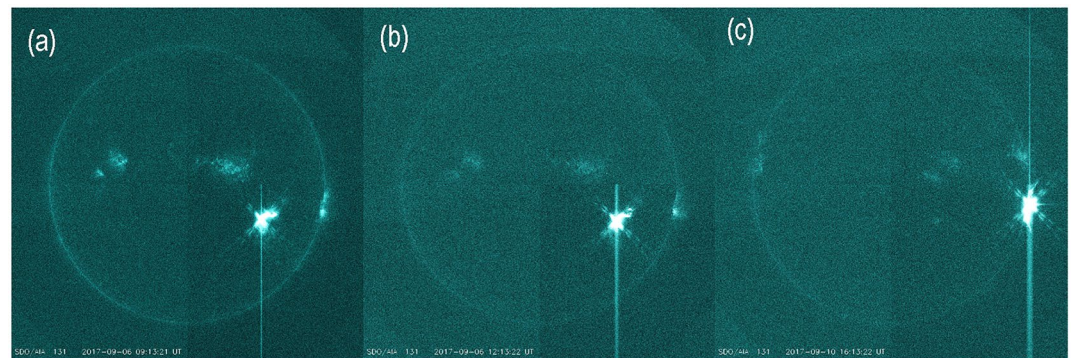


Figure 9. Location of SFs on the solar disk: (a) the X2.2 SF on 6 September 2017, (b) the X9.3 SF on 6 September 2017, and (c) the X8.2 SF on 10 September 2017 (Courtesy of NASA/SDO and the AIA, EVE, and HMI science teams from <https://sdo.gsfc.nasa.gov/>).

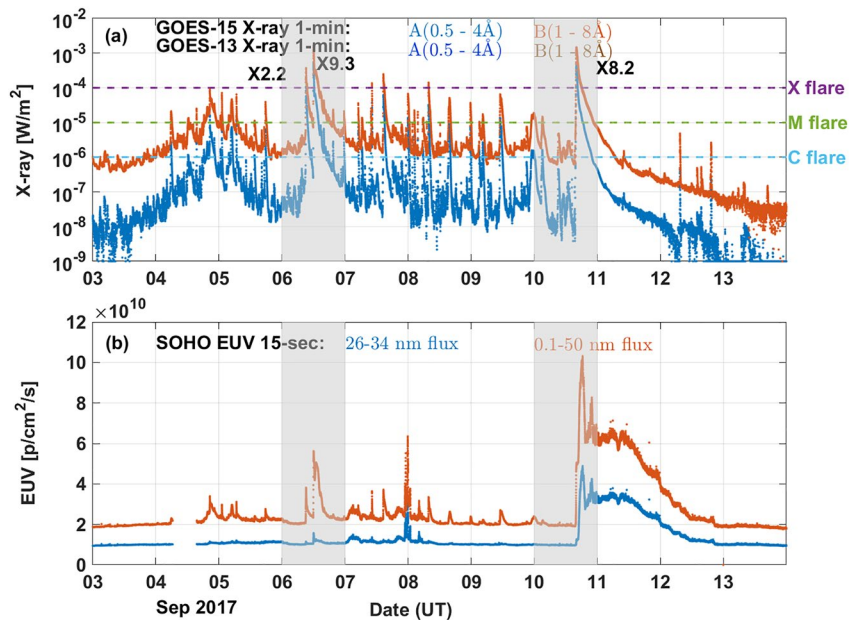


Figure 10. SF indexes from 3 September 2017 to 13 September 2017. (a) The X-ray flux from the GOES observations and (b) the EUV from the Solar Heliospheric Observatory (SOHO) observations (<https://dornsifecms.usc.edu/space-sciences-center/download-sem-data/>). The shaded areas highlight the day of September 6 and September 10 when the X-class SF events occurred.

the 9.3 disk flare on 6 September 2017. Therefore, in the case of the X8.2 SF, the intensity of the EUV radiation might not be attributed to the low ROTI variations of the ionosphere responses.

In addition, according to the model simulations in Qian et al. (2011), SFs with similar magnitudes and Sun locations generated variable responses in the thermosphere and ionosphere. In particular, the rise time and decay time of SFs were important factors in determining the responses. Specifically, increasing the decay time of the control SF had a large effect in enhancing the thermosphere and ionosphere responses, whereas reducing the rise time of the control SF had a relatively small effect in weakening the responses.

In the present study, the occurrence time of the SFs is presented in Table 2. The duration and decay time of the X8.2 SF lasted for 56 and 25 min, whereas those of the X9.3 SF were about 17 and 8 min. Although the decay time of the X8.2 SF was longer than that of the X9.3 SF, the ionospheric response to the X8.2 SF was much weaker than that to the X9.3 SF, which is different to the simulation results in Qian et al. (2011). Therefore, we deduced that the SF energy may be liberated with longer duration and decay time, leading to the weak ionospheric response to the X8.2 SF.

Qian et al. (2019) discussed the SF and geomagnetic storm effects on the thermosphere and Ionosphere during 6–11 September 2017. It was found that, from the point of the TEC variation, the maximum TEC increases during the X9.3 SF and X8.2 SF were very similar, reaching a magnitude of about 4 TECU. Thus, the ionosphere responses to the X8.2 SF presented in Qian et al. (2019) and the present study are quite different. This discrepancy might be attributed to the metrics used. The TEC metric was adopted by Qian et al. (2019), while the vROT and ROTI metrics were used in this study. The TEC data were the standard vertical TEC data product binned into 1° latitude by 1° longitude with a 5-min resolution from the Coupling, Energetics, and Dynamics of Atmospheric Regions (CEDAR) Madrigal database at <http://cedar.openmadrigal.org>. On the one hand, the slant TEC data were retrieved by leveling the large-noise pseudorange measurements with the high-accuracy carrier-phase measurements (Ciraolo et al., 2007; Nie, Xu, Rovira-Garcia, Juan Zornoza, et al., 2018). On the other hand, the vertical TEC data were projected from the slant TEC data (M. Li et al., 2018; W. Li et al., 2018). Therefore, the accuracy of the vertical TEC data was reduced by both the leveling and projecting errors. In comparison, the relative slant TEC data, as ROT in the present study, only used the high-precision carrier-phase measurements; therefore, the vROT and ROTI metrics were more sensitive to the ionosphere responses during the SF. But still, the exact factors that affect the X8.2 limb SF on 10 September 2017 remain to be discovered.

4.2. The Impacts of SFs on the Kinematic PPP Error

One of the key features of the SF effects is the SID. Taking the X9.3 SF in Figure 3 as an example, the vROT fluctuation increased from around 0.1 TECU/min before the eruption to around 1.5 TECU/min when the eruption reached the maximum. The impact of the SID on the positioning depends on the number of frequencies involved in the computation. On the one hand, the single frequency positioning will suffer seriously because the SID cannot be modeled precisely by broadcast models, such as the Klobuchar model (Klobuchar, 1987), or the post-processing models, such as the global ionosphere maps computed by the IGS (Hernández-Pajares et al., 2009; Nie, Xu, Rovira-Garcia, Zornoza, et al., 2018; Ren et al., 2016). On the other hand, the refraction effects of the ionospheric delay error (including the SID) can be mitigated by up to 99.9% through the dual-frequency IF combination (Bassiri & Hajj, 1993; Petrie et al., 2011). As shown in Table 1, the kinematic PPP solution in this study adopted the IF combination; thus, the degraded positioning accuracy presented in Figure 5 cannot be attributed to the SF-induced TEC increase directly.

The SID may have a serious impact on the pre-processing performance of the GPS observables, especially for the CS detectors. Those detectors ensure that the carrier-phase measurements do not experience discontinuities or jumps. As shown in Equation 1, the HMW combination does not contain any ionosphere delay and it is efficient at detecting large CSs despite using pseudorange observables with large noise. The PGF combination aims at detecting small CSs as it only uses high-precision carrier phase observables. However, there exists ionospheric delay effects in the PGF combination. The premise of the CS detection based on the PGF combination is that the ionosphere varies little in adjacent epochs; thus, most of the ionospheric delay effects in the PGF combination can be mitigated.

Under the default threshold, that is 0.05 m (0.48 TECU) for the PGF combination (1 m corresponds to 9.52 TECU for the PGF combination), the kinematic PPP performances presented in Figures 5 and 8, result in typical positioning accuracy at the level of 0.1–0.2 m even during the X2.2 SF. However, the positioning accuracy deteriorated during the eruption of the X9.3 SF. The reason may be that the SID rate was faster than the threshold of PGF combination divided by the sampling interval (i.e., 0.48 TECU/30 s equals 0.96 TECU/min), leading to a false of the CS detection. When the carrier-phase observables are flagged as CSs, we have to re-estimate the ambiguities as unknown parameters by increasing their noise. When multiple CSs are detected simultaneously, the number of the unknown parameters increases. Hence, the redundancy of observations decreases, ultimately weakening the estimation of all unknowns and deteriorating the positioning accuracy and stability (Nie et al., 2022a, 2022b). To verify such hypothesis, we loosen the CS threshold of the PGF combination from 0.05 m (0.48 TECU) to 0.20 m (1.92 TECU), and the results during the X2.2, X9.3, and the X8.2 SFs were depicted from Figures 11–14.

Figure 11 depicts that the kinematic PPP errors during the X2.2 and X9.3 SFs obtained with the CS threshold of the PGF combination enlarged to 0.20 m (1.92 TECU). We can see that during the X9.3 SF, the kinematic PPP errors decreased from above 0.50 m to the typical values comprised from 0.10 to 0.20 m.

To validate the relationship between the positioning errors and the CS threshold in detail, we selected VILL as a representative station from the IGS network. The kinematic PPP solution for station VILL on 6 September 2017 with different CS thresholds are presented in Figure 12. The left and middle columns in Figure 12 depicted the kinematic PPP analysis when the PGF CS threshold was 0.05 m (0.48 TECU) and 0.20 m (1.92 TECU), respectively. Since data resolution plays an important role in the PPP errors (Bahadur & Nohutcu, 2021), the kinematic PPP solution for VILL with a high-rate data sampling of 1 s is presented in the right column of Figure 12. Beneficial from the high-rate sampling data, we computed the amplitude index (S4) according to the suggested Mrak et al. (2020) and Luo et al. (2020), using the signal-to-noise ratio (SNR) observations.

Figure 12a depicts a notable positioning degradation during the X9.3 SF at about 12:00, simultaneous with large ROTI values. A previous weak ROTI variation occurs at about 09:00 during the X2.2 SF, but the accuracy of the kinematic PPP maintains the typical accuracy at the level of 0.1 m. The positioning errors are consistent with those presented in Figure 5.

The ROT fluctuations of each tracked satellite from VILL are presented in Figure 12d. Satellite ROT fluctuations are below 0.1 TECU/min most of the time, except during the X2.2 and X9.3 SFs, that increase to 0.2 TECU/min and more than 1.5 TECU/min, respectively. The satellite ROT fluctuations in Figure 12d are consistent with the

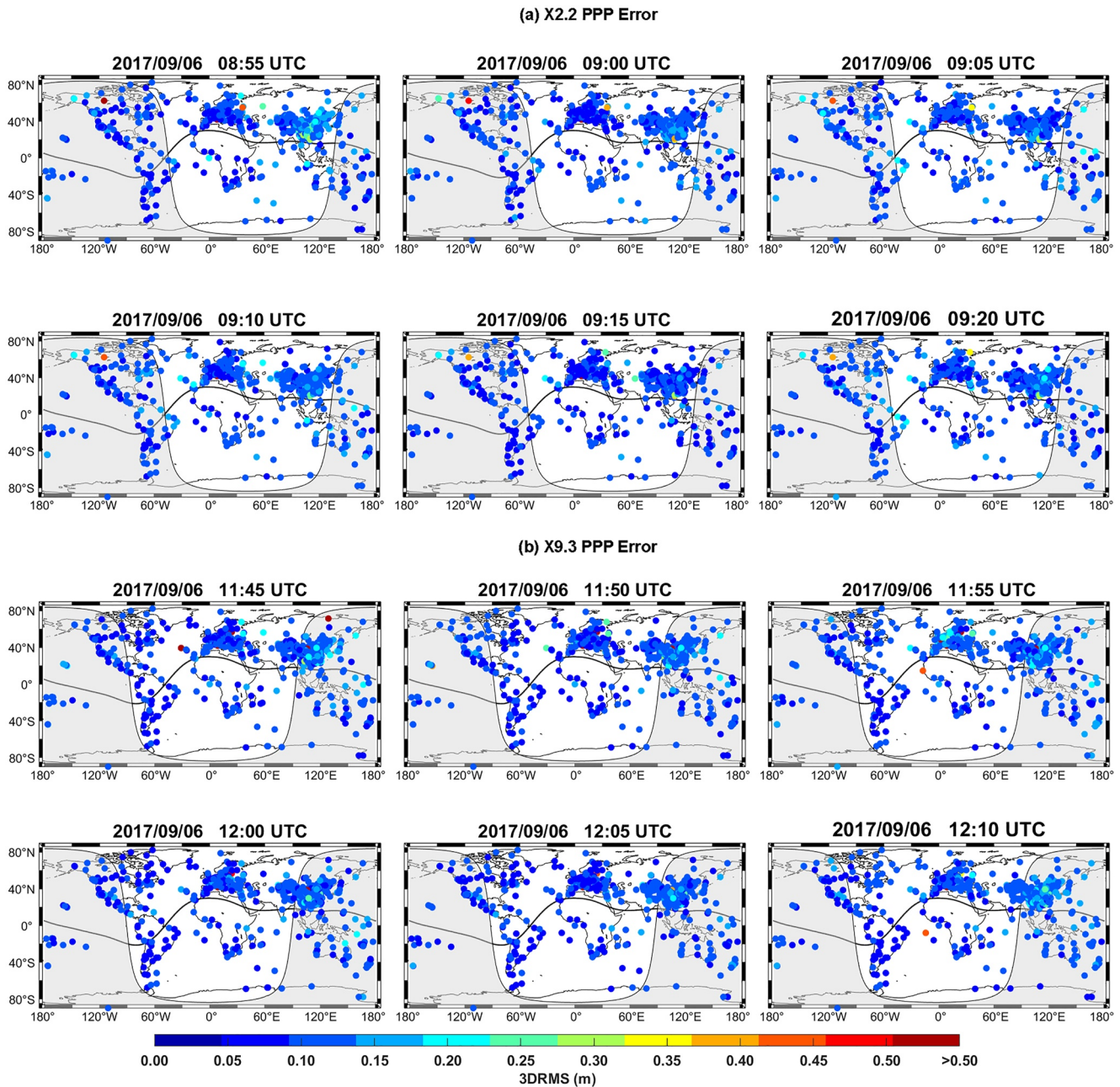


Figure 11. Snapshots of 3D kinematic PPP errors during (a) X2.2 SF and (b) X9.3 SF on 6 September 2017. The gray shading indicates nighttime. The black solid line represents the magnetic equator. In this case, the CS threshold of the PGF observable is 0.2 m (1.92 TECU).

vROT fluctuations for the station VILL in Figure 3. Figure 12j depicts the number of tracked satellites, the used satellites, the flagged CS satellites, and the excluded satellites in the kinematic PPP solution.

From Figure 12j, we can see that the receiver of VILL can track 8–10 satellites most of the time, and most of the tracked satellites were used in the kinematic PPP solution. The position dilution of precision (PDOP) around 2 indicates a good geometry. Besides, we can see that there always existed 1–2 satellites that were flagged as CS satellites. However, during the X9.3 SF at around 12:00, we can observe that most of the used satellites were flagged as CS satellites. For example, at 11:57, all of the used six satellites were detected as CS satellites. Correspondingly, the positioning errors increased to more than 1.0 m.

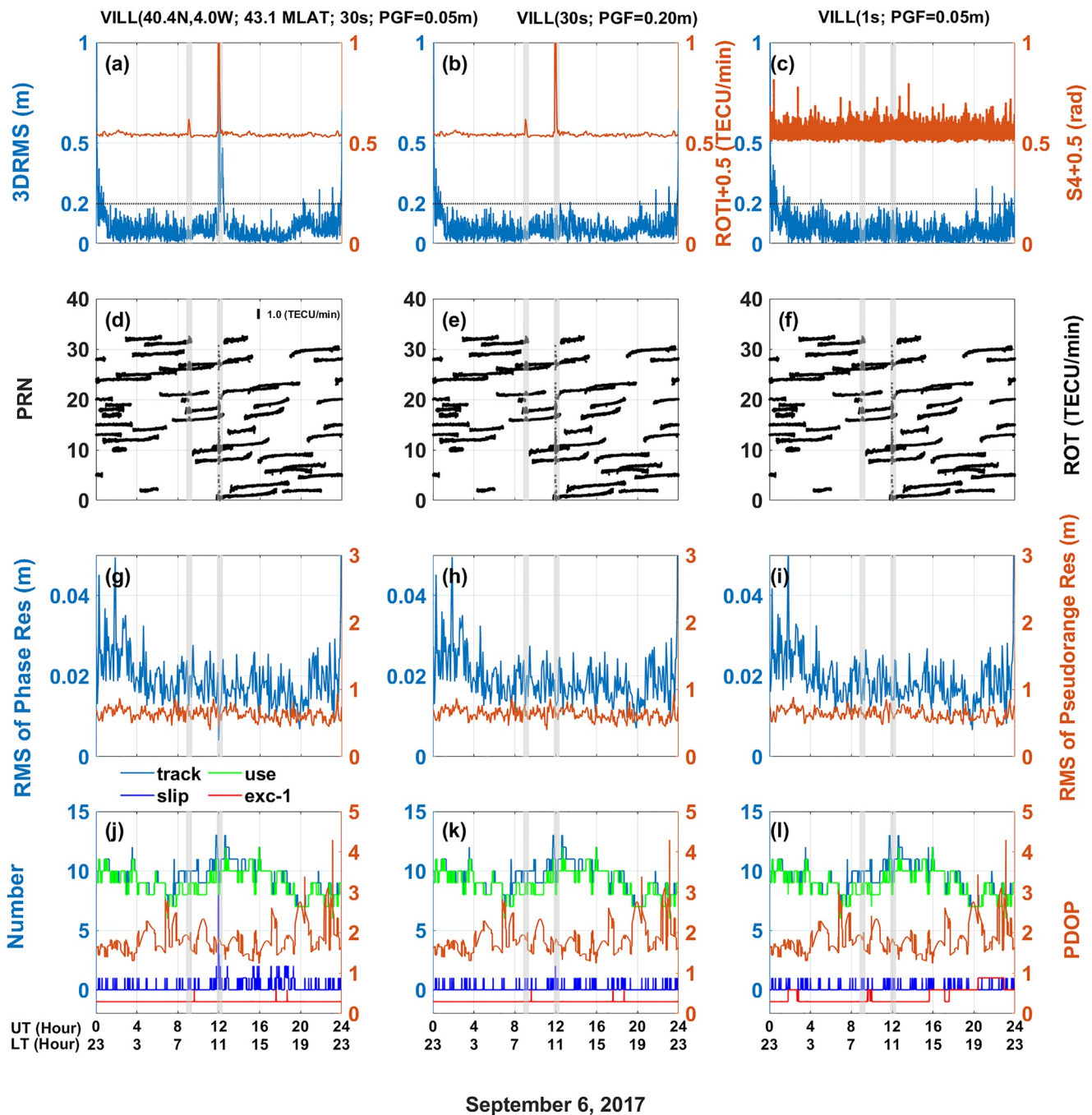


Figure 12. The kinematic PPP for station VILL on 6 September 2017 with different CS thresholds and data sampling. The results in the left column correspond to the threshold of 0.05 m (0.48 TECU), while those in the middle column correspond to the threshold of 0.20 m (1.92 TECU) with a data sampling of 30 s. The results in the right column represent the threshold of 0.05 m with a high-rate data sampling of 1 s. The two shaded area represents the eruption time of the X2.2 and X9.3 SF (a–c) present the 3D-RMS of the positioning accuracy and the ROTI or S4 variations; (d–f) present the ROT fluctuation for the different satellites separated by the Pseudorandom Number (PRN); (g–i) present the 5-min RMS of carrier-phase and pseudorange residuals of the PPP solutions; (j–l) present the number satellites tracked, used in the solution and flagged with CSs, as well as the PDOP information of the PPP solution. The track satellites represent the number of all the satellites that tracked by the receiver, the used satellites represent the number of the satellites used in the solution, the slip satellites represent the number of the detected CS satellites, and the excluded satellites represent the number of satellites that excluded from the solution due to the large residuals.

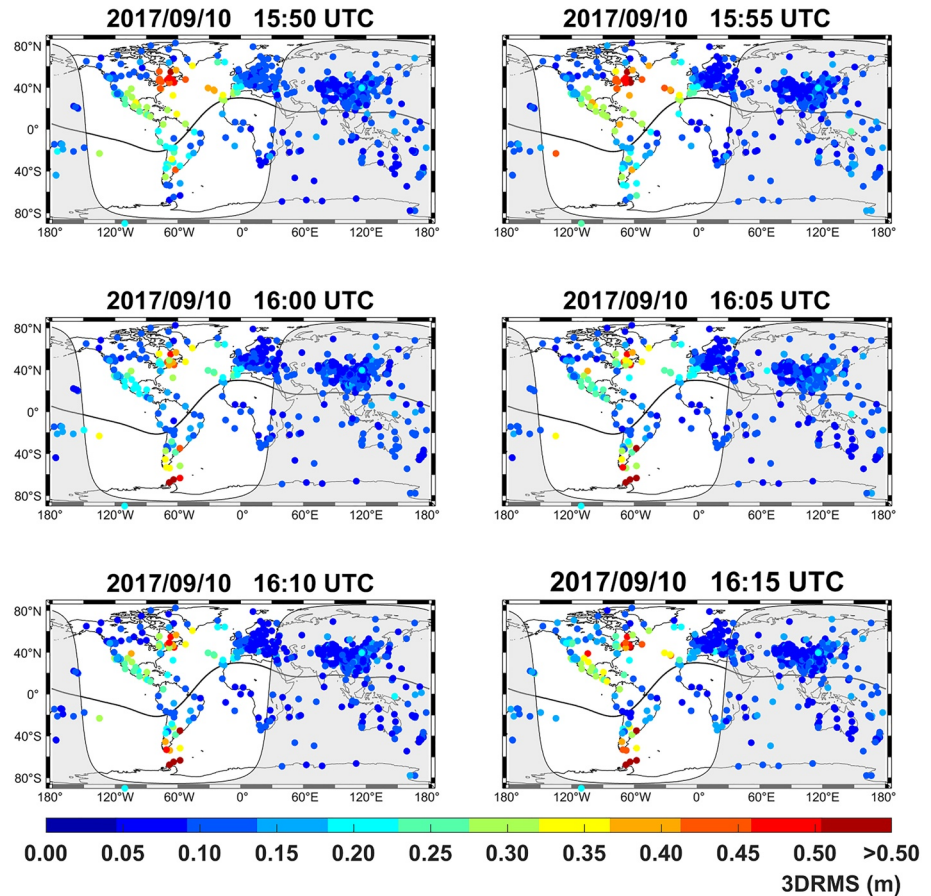


Figure 13. Snapshots of 3D kinematic PPP errors during the X8.2 SF on 10 September 2017. The gray shade indicates the nightside. The black solid line represents the magnetic equator. In this case, the CS threshold of the PGF observable is 0.2 m (1.92 TECU).

From the ROT fluctuations in Figure 12d, we deduce that the epoch-wise ionosphere variation ΔI (i.e., ROT) was around 0.20 TECU/min and 1.50 TECU/min (i.e., 0.10 TECU and 0.75 TECU every two consecutive epochs of 30 s) during the X2.2 SF and X9.3 SF. Therefore, the threshold of the PGF observable $\Delta\phi_{\text{PGF}}$ should be larger than 0.10 TECU and 0.75 TECU to cope with the rapid ionosphere variations under the SF condition. Otherwise, signals continuously tracked are falsely signaled with CS. In this regard, the commonly used PGF threshold of 0.05 m (0.48 TECU) works with the ionosphere variations during the peak eruption of the X2.2 SF but not with that of the X9.3 SF.

In comparison, Figure 12b depicts that the positioning errors did not increase during the X9.3 SF when the CS threshold of the PGF combination was 0.20 m (1.92 TECU). Especially, comparing Figure 12j with Figure 12k, the most remarkable difference between them is the number of the satellites flagged with CS. Indeed, in Figure 12k, most of the satellites during the whole day were not flagged as CS satellites. In particular, at 11:57, all of the used 6 satellites were not flagged as CS satellites. From the positioning performance in Figures 12a and 12b, we can deduce that most of such flagged CS satellites were falsely detected due to the tight CS threshold of the PGF combination.

From Figure 12c, the positioning errors become normal using the 1-s high-rate data despite the CS threshold of the PGF combination was 0.05 m (0.48 TECU). We also notice that the distribution of the amplitude scintillation index S4 is below 0.2 rad most of the time, including the period of the X2.2 and X9.3 SF, which is different from the ROTI. It indicates that the amplitude scintillation does not play the role in the increased PPP errors when using the 30-s sampling data. Comparing the results in the left with those in right column, we can find that the detected CSs are much reduced when using the high-rate sampling data, indicating that it is much easier to eliminate erroneous CSs in higher resolution data. Therefore, we conclude that the kinematic PPP solution is very

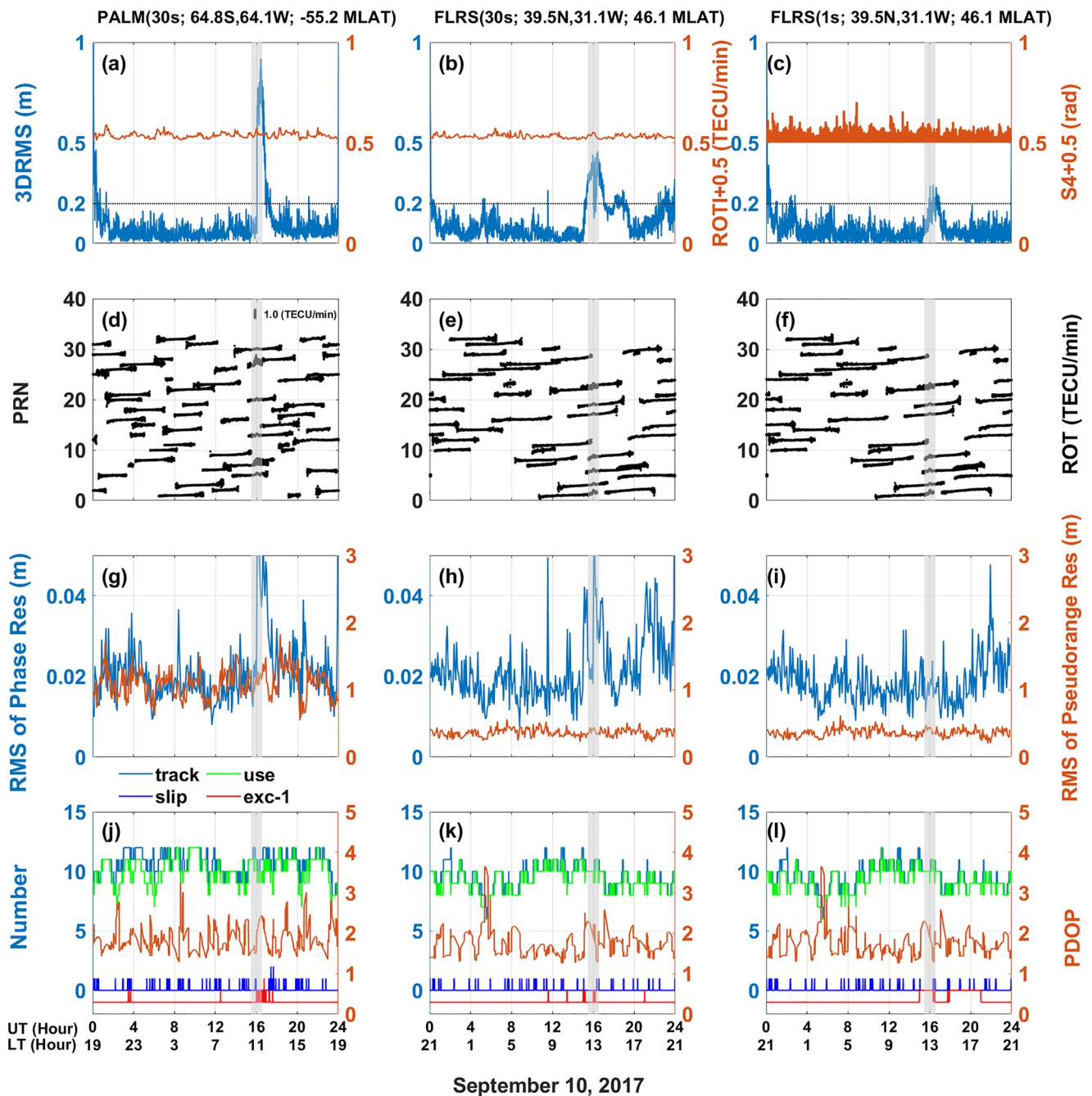


Figure 14. The kinematic PPP for station PALM (left panel) and FLRS (middle and right panels) on 10 September 2017 under the threshold of 0.20 m (1.92 TECU) for the PGF combination. The data sampling in left and middle columns is 30 s, while that in the right column is 1 s. The shaded area represents the time of the X8.2 SF (a–c) present the 3D-RMS of the positioning accuracy and the ROTI or S4 variations; (d–f) present the ROT fluctuation for the different satellites separated by the PRN; (g–i) present the 5-min RMS of the carrier-phase and pseudorange residuals of the PPP solutions; (j–l) present the number of the tracked satellites, the used satellites in the solution, the satellites with CSs and the satellites that excluded from the PPP solution, as well as the PDOP information of the PPP solution, which have the same meaning as those in Figure 12.

sensitive to CSs, which are difficult to detect in 30-s data. On the other hand, the CS detection using the high-rate sampling data is more robust for the kinematic PPP solution.

From Figures 11 and 12, we deduce that most of the SID effects on the dual-frequency positioning can be mitigated quite well by optimizing the threshold of the CS detection observables, especially for the PGF combination. However, for the positioning accuracy degradation during the X8.2 SF on 10 September 2017, the optimization

of the CS threshold of the PGF combination did not produce positive results as presented in Figures 13 and 14. Comparing Figure 13 with Figure 8, we can see that the magnitude and distribution of the PPP errors during the X8.2 SF presented minor differences under the different thresholds of the CS detection observables.

In order to analyze the mechanism behind the positioning degradation, we selected two representative stations, PALM and FLRS, from the IGS network. The kinematic PPP for stations PALM (left column) and FLRS (middle and right column) on 10 September 2017 under the threshold of 0.20 m (1.92 TECU) for the PGF combination were presented in Figure 14. The data sampling in left and middle columns is 30 s, while that in the right column is 1 s. Similarly, the amplitude index S4 for station FLRS was computed using the high-rate sampling data.

From Figures 14a and 14b, we can see that the positioning errors of both stations increased to more than 0.5 m during the X8.2 SF. However, no apparent ROTI variations are observed. Indeed, ROT fluctuations of each tracked satellite, as presented in Figures 14d and Figure 14e, remained below 0.1 TECU/min most of the time, which are consistent with the results presented in Figure 6. This may explain the reason that the positioning errors did not change with different thresholds of 0.05 and 0.20 m for the PGF combination. In the case of the X8.2 SF event, the ionospheric effect, as represented by the ROT fluctuations of each satellites, was small at the same level of the X2.2 SF due to the limb effect of the X8.2 SF. Therefore, the customary threshold of 0.05 m was adequate to cope the SID rate of both the X2.2 and X8.2 SF, let alone the threshold of 0.20 m.

As for the mechanism behind the positioning degradation during the X8.2 SF, we assessed the 5-min Root Mean Square (RMS) of the carrier-phase and pseudorange residuals depicted in Figures 14g and 14h. Since the precision of the GPS carrier-phase measurement is about 100 times higher than that of the pseudorange measurement, the residuals of the carrier-phase measurement are more critical to the accuracy of the kinematic PPP solution. From Figures 14g and 14h, we notice the significant increase of the RMS of the carrier-phase residuals, simultaneously with large positioning errors. In comparison, the RMS of the carrier-phase residuals was stable during the X2.2 and X9.3 SF as presented in Figures 12g and 12h. In fact, the carrier-phase and pseudorange residuals of the PPP solutions can reflect the precision of the corresponding GPS measurements (Juan et al., 2017). Therefore, the increase of the carrier-phase residuals may suggest that the accuracy of the GPS carrier-phase measurements was affected during the X8.2 SF. The accuracy degradation of the GPS carrier-phase measurements can also be revealed from Figures 14j and 14k, from which we can see that some satellites are excluded from the solution. The reason for such exclusion is for satellites with carrier-phase residuals larger than 4 times of its variance. This satellite exclusion occurs frequently at stations PALM and FLRS during the X8.2 SF. It is noted that though the data sampling is increased from 30 to 1 s, the positioning accuracy during the X8.2 SF can still be affected as shown in Figure 14c. Since the degraded accuracy of the GNSS measurement cannot be mitigated by the improvement of the data resolution, the positioning errors still exist.

As presented in Figure 2, the X8.2 SF on 10 September 2017 occurred during the recovery phase of the geomagnetic storm. The combined effects of the magnetic field disturbance and the X8.2 SF may cause the accuracy degradation of the GPS carrier-phase measurements and, consequently, the positioning accuracy.

5. Conclusions

The present study focused on the ionospheric responses during different X-class SFs, including the strongest X9.3 SF in Solar Cycle 24 on September 6–10, 2017. The v ROTI and ROTI metrics were exploited as representative indicators of the SID induced by the SFs. We discussed different factors that affected the ionosphere disturbances and then on the accuracy of the kinematic PPP positioning. For such purposes, we evaluated the estimated coordinate variations of 700+ GPS stations available worldwide. The major findings from the analysis are summarized as follows:

1. We confirm that the ionospheric response to the SF is related to the intensity level, location, and duration time of the three X-class SFs occurred in September 2017. ROTIs for the stations on the dayside can reach up to 0.2 TECU/min and 1.5 TECU/min during the maximum eruption of the different magnitude level of X2.2 and X9.3 SF, respectively. In contrast, the maximum ROTI variations during the eruption of the X8.2 SF only reach 0.2 TECU/min. Although the magnitude of the X8.2 SF was only a little weaker than that of the X9.3 SF, the X8.2 SF occurred on the limb side, whereas the X9.3 SF occurred near the center of the solar disk. In addition, the longer duration and decay time may also be attributed to the inconspicuous ionosphere responses to the X8.2 SF on 10 September 2017.

2. The SID induced by the SF can degrade the accuracy of the kinematic PPP solution on the dayside seriously. This kind of accuracy degradation can be related to the CS algorithms or the threshold of the CS detection observable. When the CS threshold of a combination containing the ionosphere effect is too tight, satellites can be falsely flagged as CS, reinitializing the ambiguity estimation in the PPP solution and deteriorating the positioning accuracy. When the CS threshold of the PGF combination from 0.05 m (0.48 TECU) to 0.20 m (1.92 TECU) is loosened, the positioning accuracy of the PPP solutions on the dayside during the X9.3 SF improved from larger than 0.50 m to the typical level of 0.10–0.20 m.
3. The combined effects of the magnetic field disturbance and the SF, as shown in the case of the X8.2 SF, can also degrade the accuracy of the kinematic PPP solution on the dayside. But the pattern of the PPP errors induced by the combined effect was different from those induced by the SID. In this case, the optimization of the CS threshold did not improve the positioning accuracy. The combined effect of the SF may deteriorate the precision of the GPS measurements, especially the carrier-phase measurement. Under these conditions, the accuracy of the positioning decreases.

The impacts of the different SFs on the ionosphere and the kinematic PPP solutions are not monotonous. For the SID effect of the different SFs on the positioning, it is suggested that the CS algorithms should be carefully developed further. Especially, the threshold should be set adaptively according to the intensity of the SF. For the combined effect of the magnetic field disturbance and the SF on the positioning, more studies are needed to improve the positioning accuracy and stability in the future.

Data Availability Statement

The raw GPS data are from <ftp://igs.ign.fr> as well as <https://cdis.nasa.gov/archive/>. The 1-min averaged X-ray data in the wavelength of 0.1–0.8 nm are observed by the Geostationary Operational Environmental Satellite (GOES) 13 as well as 15 at <http://www.swpc.noaa.gov/products/goes-x-ray-flux>. The EUV flux are from the Solar Heliospheric Observatory (SOHO) observations at <https://dornsifecms.usc.edu/space-sciences-center/download-sem-data/>. The ACE solar wind and IMF data are provided from CDAWeb at <https://cdaweb.gsfc.nasa.gov/>. The F10.7 measurements, longitudinally symmetric disturbances index in the horizontal direction H (SYM-H) and Auroral Electrojet indices, are provided by the Goddard Space Flight Center (GSFC) from <https://omniweb.gsfc.nasa.gov/>. The RTKLIB package (version 2.4.3 b34) for the positioning performances is provided at <http://www.rtklib.com/>.

References

- Afraimovich, E. L., Demyanov, V. V., Ishin, A. B., & Smolkov, G. Y. (2008). Powerful solar radio bursts as a global and free tool for testing satellite broadband radio systems, including GPS–GLONASS–GALILEO. *Journal of Atmospheric and Solar-Terrestrial Physics*, *70*(15), 1985–1994. <https://doi.org/10.1016/j.jastp.2008.09.008>
- Alfonsi, L., Cesaroni, C., Spogli, L., Regi, M., Paul, A., Ray, S., et al. (2021). Ionospheric disturbances over the Indian sector during 8 September 2017 geomagnetic storm: Plasma structuring and propagation. *Space Weather*, *19*(3), e2020SW002607. <https://doi.org/10.1029/2020sw002607>
- Bahadur, B., & Nohutcu, M. (2021). Impact of observation sampling rate on Multi-GNSS static PPP performance. *Survey Review*, *53*(378), 206–215. <https://doi.org/10.1080/00396265.2019.1711346>
- Bassiri, S., & Hajj, G. A. (1993). Higher-order ionospheric effects on the global positioning system observables and means of modeling them. *Manuscripta Geodaetica*, *18*(5), 280–280.
- Berdermann, J., Kriegel, M., Banyš, D., Heymann, F., Hoque, M., Wilken, V., et al. (2018). Ionospheric response to the X9.3 Flare on 6 September 2017 and its implication for navigation services over Europe. *Space Weather*, *16*(10), 1604–1615. <https://doi.org/10.1029/2018SW001933>
- Bertiger, W., Bar-Sever, Y., Dorsey, A., Haines, B., Harvey, N., Hemberger, D., et al. (2020). GipsyX/RTGx, a new tool set for space geodetic operations and research. *Advances in Space Research*, *66*(3), 469–489. <https://doi.org/10.1016/j.asr.2020.04.015>
- Blagoveshchensky, D. V., & Sergeeva, M. A. (2019). Impact of geomagnetic storm of September 7–8, 2017 on ionosphere and HF propagation: A multi-instrument study. *Advances in Space Research*, *63*(1), 239–256. <https://doi.org/10.1016/j.asr.2018.07.016>
- Blewitt, G. (1990). An automatic editing algorithm for GPS data. *Geophysical Research Letters*, *17*(3), 199–202. <https://doi.org/10.1029/GL017i003p00199>
- Boehm, J., Niell, A. E., Tregoning, P., & Schuh, H. (2006). Global Mapping Function (GMF): A new Empirical mapping Function based on data from Numerical weather model data. *Geophysical Research Letters*, *33*(7), L07304. <https://doi.org/10.1029/2005GL025546>
- Carrano, C. S., Bridgwood, C. T., & Groves, K. M. (2009). Impacts of the December 2006 solar radio bursts on the performance of GPS. *Radio Science*, *44*(1). <https://doi.org/10.1029/2008RS004071>
- Cerruti, A. P., Kintner, P. M., Gary, D. E., Lanzerotti, L. J., De Paula, E. R., & Vo, H. B. (2006). Observed solar radio burst effects on GPS/Wide Area Augmentation System carrier-to-noise ratio. *Space Weather*, *4*(10), S10006. <https://doi.org/10.1029/2006SW000254>
- Chen, Z., Gao, Y., & Liu, Z. (2005). Evaluation of solar radio bursts' effect on GPS receiver signal tracking within International GPS Service network. *Radio Science*, *40*(3), RS3012. <https://doi.org/10.1029/2004RS003066>
- Cheng, N., Song, S., & Xie, H. (2018). Investigation of solar flares impact on GPS/BDS/GALILEO broadcast ionospheric models. *Radio Science*, *54*(1), 91–103. <https://doi.org/10.1029/2018rs006591>

Acknowledgments

The study is funded by National Natural Science Foundation of China (Nos. 42004012 and 42004025), Natural Science Foundation of Shandong Province, China (No. ZR2020QD048), State Key Laboratory of Geo-Information Engineering (No. SKLGIE2019-Z-2-2), State Key Laboratory of Geodesy and Earth's Dynamics (No. SKLGED-2021-3-4), and by the project RTI2018-094295-B-I00 funded by the MCIN/AEI 10.13039/501100011033, which is cofunded by the FEDER programme. We appreciate the discussion on the amplitude scintillation and IF-sigma from high-rate geodetic GNSS data with Dr. Xiaomin Luo from China University of Geosciences (Wuhan) and Prof. Juan, J. M. from Universitat Politècnica de Catalunya (UPC), Spain. The authors are also thankful to the reviewers for the instructive comments and suggestions on the manuscript.

- Cherniak, I., Zakharenkova, I., & Krankowski, A. (2014). Approaches for modeling ionosphere irregularities based on the TEC rate index. *Earth, Planets and Space*, 66(1), 165. <https://doi.org/10.1186/s40623-014-0165-z>
- Ciraolo, L., Azpilicueta, F., Brunini, C., Meza, A., & Radicella, S. M. (2007). Calibration errors on experimental slant total electron content (TEC) determined with GPS. *Journal of Geodesy*, 81(2), 111–120. <https://doi.org/10.1007/s00190-006-0093-1>
- Dach, R., Lutz, S., Walser, P., & Fridez, P. (2015). *Bernese GNSS software version 5.2*. University of Bern, Bern Open Publishing. <https://doi.org/10.7892/boris.72297>
- Demyanov, V., & Yasyukevich, Y. V. (2021). Space weather: Risk factors for global navigation satellite systems. *Solar-Terrestrial Physics*, 7(2), 28–47. <https://doi.org/10.12737/stp-72202104>
- Desai, M. V., & Shah, S. N. (2020). Overview of the influence of X2.2 and X9.3 solar flares on NavIC system. *Acta Geodaetica et Geophysica*, 55(4), 567–577. <https://doi.org/10.1007/s40328-020-00316-2>
- Dey, A., Joshi, L. M., Chhibba, R., & Sharma, N. (2021). A study of ionospheric effects on IRNSS/NavIC positioning at equatorial latitudes. *Advances in Space Research*, 68(12), 4872–4883. <https://doi.org/10.1016/j.asr.2020.09.038>
- Donnelly, R. (1976). Empirical models of solar flare X ray and EUV emission for use in studying their E and F region effects. *Journal of Geophysical Research*, 81(25), 4745–4753. <https://doi.org/10.1029/JA081i025p04745>
- Fagundes, P. R., Pezzopane, M., Habarulema, J., Venkatesh, K., Dias, M., Tardelli, A., et al. (2020). Ionospheric disturbances in a large area of the terrestrial globe by two strong solar flares of September 6, 2017, the strongest space weather events in the last decade. *Advances in Space Research*, 66(7), 1775–1791. <https://doi.org/10.1016/j.asr.2020.06.032>
- Hatch, R. (1983). The synergism of GPS code and carrier measurements. In *International Geodetic Symposium on Satellite Doppler Positioning* (Vol. 2, pp. 1213–1231).
- Hernández-Pajares, M., Juan, J., Sanz, J., Orus, R., Garcia-Rigo, R., Felten, J., et al. (2009). The IGS VTEC maps: A reliable source of ionospheric information since 1998. *Journal of Geodesy*, 83(3–4), 263–275. <https://doi.org/10.1007/s00190-008-0266-1>
- Hernández-Pajares, M., Juan, J., Sanz, J., & Solé, J. (1998). Global observation of the ionospheric electronic response to solar events using ground and LEO GPS data. *Journal of Geophysical Research*, 103(A9), 20789–20796. <https://doi.org/10.1029/98JA01272>
- Imtiaz, N., Younas, W., & Khan, M. (2020). Response of the low- to mid-latitude ionosphere to the geomagnetic storm of September 2017. *Annales Geophysicae*, 38(2), 359–372. <https://doi.org/10.5194/angeo-38-359-2020>
- Juan, J. M., Aragon-Angel, A., Sanz, J., González-Casado, G., & Rovira-García, A. (2017). A method for scintillation characterization using geodetic receivers operating at 1 Hz. *Journal of Geodesy*, 91(11), 1383–1397. <https://doi.org/10.1007/s00190-017-1031-0>
- Juan, J. M., Sanz, J., Rovira-García, A., González-Casado, G., Ibáñez, D., & Perez, R. O. (2018). AATR an ionospheric activity indicator specifically based on GNSS measurements. *Journal of Space Weather and Space Climate*, 8, A14. <https://doi.org/10.1051/swsc/2017044>
- Klobuchar, J. A. (1987). Ionospheric time-delay algorithm for single-frequency GPS users. *IEEE Transactions on Aerospace and Electronic Systems*, 3, 325–331. <https://doi.org/10.1109/TAES.1987.310829>
- Kumar, S., & Kumar, S. (2020). Equatorial ionospheric TEC and scintillations under the space weather events of 4–9 September 2017: M-class solar flares and a G4 geomagnetic storm. *Journal of Atmospheric and Solar-Terrestrial Physics*, 209, 105421. <https://doi.org/10.1016/j.jastp.2020.105421>
- Le, H., Liu, L., Chen, Y., & Wan, W. (2013). Statistical analysis of ionospheric responses to solar flares in the solar cycle 23. *Journal of Geophysical Research: Space Physics*, 118(1), 576–582. <https://doi.org/10.1029/2012ja017934>
- Le, H., Liu, L., Ren, Z., Chen, Y., Zhang, H., & Wan, W. (2016). A modeling study of global ionospheric and thermospheric responses to extreme solar flare. *Journal of Geophysical Research: Space Physics*, 121(1), 832–840. <https://doi.org/10.1002/2015JA021930>
- Lei, J., Huang, F., Chen, X., Zhong, J., Ren, D., Wang, W., et al. (2018). Was magnetic storm the only driver of the Long-duration enhancements of Daytime total electron content in the Asian-Australian sector between 7 and 12 September 2017? *Journal of Geophysical Research: Space Physics*, 123(4), 3217–3232. <https://doi.org/10.1029/2017ja025166>
- Li, M., Yuan, Y., Zhang, B., Wang, N., Li, Z., Liu, X., & Zhang, X. (2018). Determination of the optimized single-layer ionospheric height for electron content measurements over China. *Journal of Geodesy*, 92(2), 169–183. <https://doi.org/10.1007/s00190-017-1054-6>
- Li, W., Yue, J., Yang, Y., He, H., Hu, A., & Zhang, K. (2018). Ionospheric and thermospheric responses to the recent strong solar flares on 6 September 2017. *Journal of Geophysical Research: Space Physics*, 123(10), 8865–8883. <https://doi.org/10.1029/2018ja025700>
- Li, X., Ge, M., Dai, X., Ren, X., Fritsche, M., Wickert, J., & Schuh, H. (2015). Accuracy and reliability of multi-GNSS real-time precise positioning: GPS, GLONASS, BeiDou, and Galileo. *Journal of Geodesy*, 89(6), 607–635. <https://doi.org/10.1007/s00190-015-0802-8>
- Linty, N., Minetto, A., Dovis, F., & Spogli, L. (2018). Effects of phase scintillation on the GNSS positioning error during the September 2017 storm at Svalbard. *Space Weather*, 16(9), 1317–1329. <https://doi.org/10.1029/2018sw001940>
- Liu, J., & Ge, M. (2003). PANDA software and its preliminary result of positioning and orbit determination. *Wuhan University Journal of Natural Sciences*, 8(2), 603–609. <https://doi.org/10.1007/BF02899825>
- Liu, J., Wang, W., Qian, L., Lotko, W., Burns, A. G., Pham, K., et al. (2021). Solar flare effects in the Earth's magnetosphere. *Nature Physics*, 17(7), 807–812. <https://doi.org/10.1038/s41567-021-01203-5>
- Liu, L., Wan, W., Chen, Y., & Le, H. (2011). Solar activity effects of the ionosphere: A brief review. *Chinese Science Bulletin*, 56(12), 1202–1211. <https://doi.org/10.1007/s11434-010-4226-9>
- Liu, L., Zou, S., Yao, Y., & Aa, E. (2020). Multi-scale ionosphere responses to the May 2017 magnetic storm over the Asian sector. *GPS Solutions*, 24(1), 26. <https://doi.org/10.1007/s10291-019-0940-1>
- Luo, X., Gu, S., Lou, Y., Cai, L., & Liu, Z. (2020). Amplitude scintillation index derived from C/N0 measurements released by common geodetic GNSS receivers operating at 1 Hz. *Journal of Geodesy*, 94(2), 1–14. <https://doi.org/10.1007/s00190-020-01359-7>
- Lyard, F., Lefevre, F., Letellier, Y., & Francis, O. (2006). Modelling the global ocean tides: Modern insights from FES2004. *Ocean Dynamics*, 56(5–6), 394–415. <https://doi.org/10.1007/s10236-006-0086-x>
- Melbourne, W. (1985). The case for ranging in GPS-based geodetic systems. In *Proceedings of the 1st International Symposium on Precise Positioning with the Global Positioning System* (pp. 373–386).
- Mitra, A. P. (1974). Ionospheric effects of solar flares. In *Astrophysics and Space Science Library* (Vol. 46). <https://doi.org/10.1007/978-94-010-2231-6>
- Mrak, S., Semeter, J., Nishimura, Y., Rodrigues, F. S., Coster, A. J., & Groves, K. (2020). Leveraging geodetic GPS receivers for ionospheric scintillation science. *Radio Science*, 55(11), 1–17. <https://doi.org/10.1029/2020RS007131>
- Nie, W., Rovira-García, A., Li, M., Fang, Z., Wang, Y., Zheng, D., & Xu, T. (2022). The mechanism for GNSS-based kinematic positioning degradation at high-latitudes under the March 2015 great storm. *Space Weather*, 20(6), e2022SW003132. <https://doi.org/10.1029/2022SW003132>
- Nie, W., Wang, Y., Rovira-García, A., Zheng, D., & Xu, T. (2022). Effect of the polar cap ionospheric sporadic-E layer on GNSS-based positioning: A case study at Resolute Bay, Canada, September 5, 2012. *GPS Solutions*, 26(2), 60. <https://doi.org/10.1007/s10291-022-01246-y>

- Nie, W., Xu, T., Rovira-García, A., Juan Zornoza, J. M., Sanz Subirana, J., González-Casado, G., et al. (2018). Revisit the calibration errors on experimental slant total electron content (TEC) determined with GPS. *GPS Solutions*, 22(3), 1–11. <https://doi.org/10.1007/s10291-018-0753-7>
- Nie, W., Xu, T., Rovira-García, A., Zornoza, J. M. J., Subirana, J. S., González-Casado, G., et al. (2018). The impacts of the ionospheric observable and mathematical model on the global ionosphere model. *Remote Sensing*, 10(2), 169. <https://doi.org/10.3390/rs10020169>
- Nishimura, Y., Mrak, S., Semeter, J., Coster, A., Jayachandran, P., Groves, K., et al. (2021). Evolution of mid-latitude density irregularities and scintillation in North America during the 7–8 September 2017 storm. *Journal of Geophysical Research: Space Physics*, 126(6). <https://doi.org/10.1029/2021JA029192>
- Owolabi, C., Lei, J., Bolaji, O. S., Ren, D., & Yoshikawa, A. (2020). Ionospheric Current variations induced by the solar flares of 6 and 10 September 2017. *Space Weather*, 18(11). <https://doi.org/10.1029/2020sw002608>
- Petit, G., & Luzum, B. (2010). *IERS conventions (2010)*. Bureau International des Poids et Mesures.
- Petrie, E. J., Hernández-Pajares, M., Spalla, P., Moore, P., & King, M. A. (2011). A review of higher order ionospheric refraction effects on dual frequency GPS. *Surveys in Geophysics*, 32(3), 197–253. <https://doi.org/10.1007/s10712-010-9105-z>
- Pi, X., Mannucci, A., Lindqwister, U., & Ho, C. (1997). Monitoring of global ionospheric irregularities using the worldwide GPS network. *Geophysical Research Letters*, 24(18), 2283–2286. <https://doi.org/10.1029/97GL02273>
- Pröls, G. (2012). *Physics of the Earth's space environment: An introduction*. Springer Science & Business Media.
- Qian, L., Burns, A. G., Chamberlin, P. C., & Solomon, S. C. (2010). Flare location on the solar disk: Modeling the thermosphere and ionosphere response. *Journal of Geophysical Research: Space Physics*, 115(A9), A09311. <https://doi.org/10.1029/2009ja015225>
- Qian, L., Burns, A. G., Chamberlin, P. C., & Solomon, S. C. (2011). Variability of thermosphere and ionosphere responses to solar flares. *Journal of Geophysical Research*, 116(A10), A10309. <https://doi.org/10.1029/2011ja016777>
- Qian, L., Wang, W., Burns, A. G., Chamberlin, P. C., Coster, A., Zhang, S. R., & Solomon, S. C. (2019). Solar flare and geomagnetic storm effects on the thermosphere and ionosphere during 6–11 September 2017. *Journal of Geophysical Research: Space Physics*, 124(3), 2298–2311. <https://doi.org/10.1029/2018ja026175>
- Ren, X., Zhang, X., Xie, W., Zhang, K., Yuan, Y., & Li, X. (2016). Global ionospheric modelling using multi-GNSS: BeiDou, Galileo, GLONASS and GPS. *Scientific Reports*, 6(1), 1–11. <https://doi.org/10.1038/srep33499>
- Saastamoinen, J. (1972). Contributions to the theory of atmospheric refraction. *Bulletin Geodesique*, 105(1), 279–298. <https://doi.org/10.1007/BF02521844>
- Sato, H., Jakowski, N., Berdermann, J., Jiricka, K., Heßelbarth, A., Banyas, D., & Wilken, V. (2019). Solar Radio Burst events on September 6, 2017 and its impact on GNSS signal frequencies. *Space Weather*, 17(6), 816–826. <https://doi.org/10.1029/2019SW002198>
- Sreeja, V., Aquino, M., De Jong, K., & Visser, H. (2014). Effect of the 24 September 2011 solar radio burst on precise point positioning service. *Space Weather*, 12(3), 143–147. <https://doi.org/10.1002/2013sw001011>
- Takasu, T. (2013). RTKLIB version 2.4.2 manual. *RTKLIB: An open source program package for GNSS positioning* (pp. 29–49).
- Tsurutani, B., Mannucci, A., Iijima, B., Guarnieri, F., Gonzalez, W., Judge, D., et al. (2006). The extreme Halloween 2003 solar flares (and Bastille Day, 2000 flare), ICMes, and resultant extreme ionospheric effects: A review. *Advances in Space Research*, 37(8), 1583–1588. <https://doi.org/10.1016/j.asr.2005.05.114>
- Tsurutani, B. T., Verkhoglyadova, O. P., Mannucci, A. J., Lakhina, G. S., Li, G., & Zank, G. P. (2009). A brief review of “solar flare effects” on the ionosphere. *Radio Science*, 44(1). <https://doi.org/10.1029/2008rs004029>
- Wubben, G. (1985). Software developments for geodetic positioning with GPS using TI 4100 code and carrier measurements. In *Proceedings 1st International Symposium on Precise Positioning with the Global Positioning System* (pp. 403–412).
- Xiong, B., Wan, W., Liu, L., Withers, P., Zhao, B., Ning, B., et al. (2011). Ionospheric response to the X-class solar flare on 7 September 2005. *Journal of Geophysical Research*, 116(A11), A11317. <https://doi.org/10.1029/2011JA016961>
- Yamauchi, M., Sergienko, T., Enell, C. F., Schillings, A., Slapak, R., Johnsen, M. G., et al. (2018). Ionospheric response observed by EISCAT during the 6–8 September 2017 space weather event: Overview. *Space Weather*, 16(9), 1437–1450. <https://doi.org/10.1029/2018sw001937>
- Yang, Z., & Liu, Z. (2016). Correlation between ROTI and ionospheric scintillation indices using Hong Kong low-latitude GPS data. *GPS Solutions*, 20(4), 815–824. <https://doi.org/10.1007/s10291-015-0492-y>
- Yang, Z., Morton, Y. T. J., Zakharenkova, I., Cherniak, I., Song, S., & Li, W. (2020). Global view of ionospheric disturbance impacts on kinematic GPS positioning solutions during the 2015 St. Patrick's Day storm. *Journal of Geophysical Research: Space Physics*, 125(7), e2019JA027681. <https://doi.org/10.1029/2019ja027681>
- Yasyukevich, Y., Astafeyeva, E., Padokhin, A., Ivanova, V., Syrovatskii, S., & Podlesnyi, A. (2018). The 6 September 2017 X-class solar flares and their impacts on the ionosphere, GNSS, and HF radio wave propagation. *Space Weather*, 16(8), 1013–1027. <https://doi.org/10.1029/2018SW001932>
- Zakharenkova, I., & Cherniak, I. (2021). Effects of storm-induced equatorial plasma bubbles on GPS-based kinematic positioning at equatorial and middle latitudes during the September 7–8, 2017, geomagnetic storm. *GPS Solutions*, 25(4), 132. <https://doi.org/10.1007/s10291-021-01166-3>
- Zhang, D., Mo, X., Cai, L., Zhang, W., Feng, M., Hao, Y., & Xiao, Z. (2011). Impact factor for the ionospheric total electron content response to solar flare irradiation. *Journal of Geophysical Research*, 116(A4), A04311. <https://doi.org/10.1029/2010JA016089>
- Zhang, D., Xiao, Z., & Chang, Q. (2002). The correlation of flare's location on solar disc and the sudden increase of total electron content. *Chinese Science Bulletin*, 47(1), 83–85. <https://doi.org/10.1360/02tb9017>
- Zhang, S.-R., Erickson, P. J., Coster, A. J., Rideout, W., Vierinen, J., Jonah, O., & Goncharenko, L. P. (2019). Subauroral and polar traveling ionospheric disturbances during the 7–9 September 2017 storms. *Space Weather*, 17(12), 1748–1764. <https://doi.org/10.1029/2019SW002325>
- Zhang, X., Guo, F., & Zhou, P. (2014). Improved precise point positioning in the presence of ionospheric scintillation. *GPS Solutions*, 18(1), 51–60. <https://doi.org/10.1007/s10291-012-0309-1>